

T.G. Carrell · A.M. Tyryshkin · G.C. Dismukes

An evaluation of structural models for the photosynthetic water-oxidizing complex derived from spectroscopic and X-ray diffraction signatures

Received: 6 March 2001 / Accepted: 26 September 2001 / Published online: 8 November 2001
© SBIC 2001

Abstract Four of the five intermediate oxidation states (S-states) in the catalytic cycle of water oxidation used by O₂-evolving photoautotrophs have been previously characterized by EPR and/or ENDOR spectroscopy, with the first reports for the S₀, S₁, and S₃ states available in just the last three years. The first electron density map of the Mn cluster derived from X-ray diffraction measurements of single crystals of photosystem II at 3.8–4.2 Å resolution has also appeared this year. This wealth of new information has provided significant insight into the structure of the inorganic core (Mn₄O_x-Ca₁Cl_{1–2}), the Mn oxidation states, and the location and function of the essential Ca²⁺ cofactor within the water-oxidizing complex (WOC). We summarize these advances and provide a unified interpretation of debated structural proposals and Mn oxidation states, based on an integrated analysis of the published data, particularly from Mn X-ray absorption spectroscopy (XAS) and EPR/ENDOR data. Only three magnetic spin-exchange models for the inter-manganese interactions are possible from consideration of the EPR data for the S₀, S₁, S₂ and S_{-N} (NO-reduced) states. These models fall into one of three types denoted butterfly, funnel, or tetrahedron. A revised set of eight allowed chemical structures for the Mn₄O_x core can be deduced that are shown to be consistent with both EPR and XAS. The popular “dimer-of-dimers” structural model is not compatible with the possible structural candidates. EPR data have identified two inter-manganese couplings that are sensitive to the S-state, suggesting two possible bridging sites for substrate water molecules. Spin densities derived from ⁵⁵Mn

hyperfine data together with Mn K-edge energies from Ca-depleted samples provide an internally consistent assignment for the Mn oxidation states of Mn₄(3III,IV) for the S₂ state. EPR and XAS data also provide a consistent picture, locating Ca²⁺ as an integral part of the inorganic core, probably via shared bridging ligands with Mn (aqua/hydroxo/carboxylato/chloro). XAS data reveal that the Ca²⁺ cofactor increases the Mn(1s → 4p) transition energy by 0.6–1 eV with minimal structural perturbation versus the Ca-depleted WOC. Thus, calcium binding appears to increase the Mn-ligand covalency by increasing electron transfer from shared ligands to Mn, suggesting a direct role for Ca²⁺ in substrate water oxidation. Consideration of both the XAS and the EPR data, together with reactivity studies on two model complexes that evolve O₂, suggest two favored structure types as feasible models for the reactive S₄ state that is precursor to the O₂ evolution step. These are a calcium-capped “cuboidal” core and a calcium-capped “funnel” core.

Keywords Photosynthesis · Catalysis · Oxygen evolution · Water oxidation · Manganese

Introduction to S-state terminology

The terminology used to denote the intermediate states involved in photosynthetic water oxidation originates with the pioneering discovery by Joliot and its interpretation by Kok and their co-workers. They showed that O₂ is evolved only after removal of four electrons from a catalytic center associated with the photosystem II (PSII) reaction center of plants and algal chloroplasts ([1] and references therein). The photochemistry was shown to involve sequential one-electron steps (Fig. 1), resulting in five intermediate oxidation states that were called S-states. Later the catalytic center was shown to comprise a spin-coupled tetramanganese cluster that is part of an inorganic core denoted the PSII water-oxidizing complex (WOC) [2, 3]. The inorganic composition

Dedicated to the memory of Gerald T. Babcock, scientific pioneer and passionate communicator of nature's molecular machines

T.G. Carrell · A.M. Tyryshkin · G.C. Dismukes (✉)
Princeton University, Department of Chemistry,
Hoyt Laboratory, Princeton, NJ 08544, USA
E-mail: dismukes@princeton.edu
Tel.: +1-609-2583949
Fax: +1-609-2581980

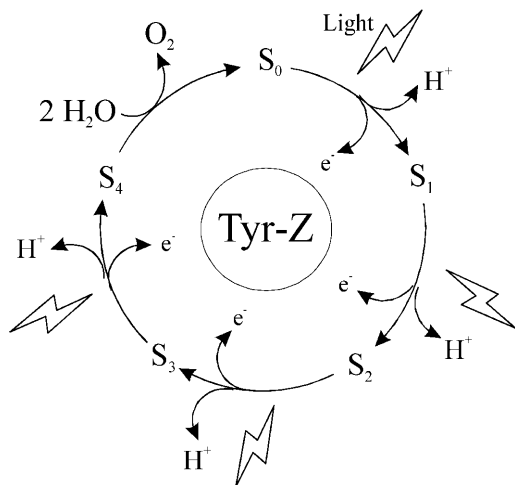


Fig. 1 S-state notation of intermediates in the photosynthetic water oxidation cycle

of the core as currently understood is $\text{Mn}_4\text{Ca}_1\text{Cl}_{1-2}\text{O}_y(\text{HCO}_3)_z$ [4, 5]. All of these native cofactors, with the possible exception of bicarbonate, are required for water splitting. Figure 1 shows also the successive release of protons during the catalytic cycle and the extraction of electrons via a photogenerated tyrosine radical, designated Y_z^\bullet , that is also known to be an integral part of the catalytic center [6]. The stoichiometry of proton release during the cycle depends on several factors. Patterns of 1-0-1-2 and 1-1-1-1 were observed and depend on the PSII source, the preparation of the sample, and pH. Electrostatic effects on ionizable protein residues contribute to the proton stoichiometry, as well as protons released from substrate water molecules. Together with the narrow pH optimum for O_2 evolution activity, these data have been taken as evidence for the thermodynamic coupling of the electron and proton currents during S-state cycling [7, 8, 9]. A histidine residue associated with the D1 subunit of PSII (His190) appears to be directly involved in interactions with Y_z^\bullet and directing the proton current [10].

The half-lives for reduction of the Y_z^\bullet radical after flash excitation of PSII ($\text{S}_n\text{Y}_z^\bullet \rightarrow \text{S}_{n+1}\text{Y}_z$; $n=0, 1, 2, 3$) are in the range of 30–1000 μs , with each successive step being threefold slower. The Mn cluster is the electron donor on at least two, if not all three, of these steps. No other redox-active species has yet been identified. The last step ($\text{S}_3\text{Y}_z^\bullet \rightarrow \text{S}_0\text{Y}_z + \text{O}_2$) is rate-limiting with a half-life of ~ 1 ms and coincides with the release of O_2 . The thermodynamic driving force for these steps decreases from $\Delta G = -24$ to -4 to -5 kJ/mol on the first three steps and -10 kJ/mol on the O_2 production step [11]. The activation energies for these steps vary between 5 and 36 kJ/mol [11]. The first two steps have smaller activation energies and were proposed to conform to Marcus theory expectations for long-range electron transfer steps, while the much larger activation barriers found on the final two steps suggest that an additional gating

mechanism may control the electron/proton transfer reactions.

Herein, we summarize data on the electronic and chemical structures of the inorganic core of the WOC. In the next section we begin with a look at the recent structural model of the manganese center of PSII based on X-ray diffraction experiments of single crystals at a resolution of 3.8–4.2 Å. We next focus attention on the debated interpretations of the more extensive spectroscopic evidence from X-ray absorption spectroscopy (XAS) and electron spin resonance techniques (EPR, ENDOR, etc.). We summarize the set of geometric structures for the Mn_4 cluster that are consistent with all three types of data and thus represent a unified structural proposal. Finally, we relate these structures to the known examples of synthetic Mn-oxo complexes that are functionally active in the evolution of O_2 . We arrive at two Mn-oxo core types that are favored candidates for the catalytic core of the WOC, based on currently available structural and functional data.

Single-crystal X-ray diffraction model of the WOC

The most informative recent development in PSII research is the report of an X-ray crystal structure of a dimeric PSII core complex from the thermophilic cyanobacterium *Synechococcus elongatus* [12]. The structure shows how most of the 17 protein subunits and their associated cofactors are spatially organized with respect to one another and the internal membrane. This work extends prior electron diffraction studies of spinach PSII complexes that were limited to 8 Å resolution [13]. The resolution of the native data set was limited to 4.2 Å. Phases were obtained from several isomorphous heavy-atom derivatives that diffract to lower resolution, and were extended to 3.8 Å using a single data set obtained from a heavy-atom derivative (Cd) and by twofold non-crystallographic averaging of the two monomers. The current model assigns 4342 atoms, or about 10% of the approximately 45,000 atoms for the complete model. The resulting crystallographic R -factor of the current model is 0.59, which together with the 3.8–4.2 Å resolution indicates there is considerable uncertainty in drawing conclusions at the atomic level of resolution without resorting to other non-crystallographic knowledge.

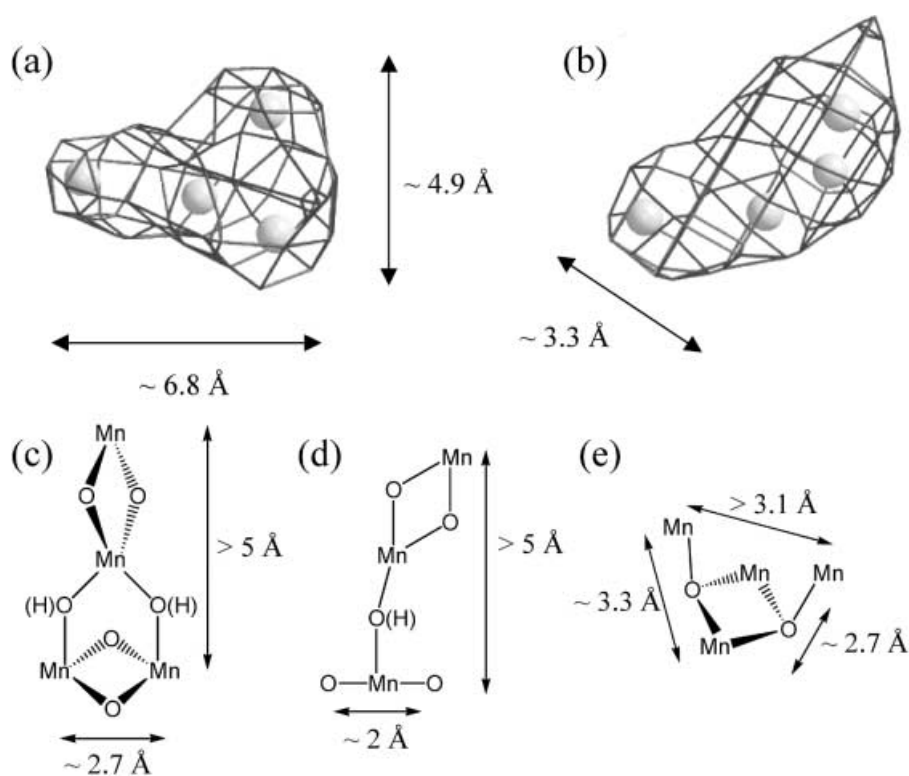
These data have provided a wealth of new information [14, 15]. The location of the Mn cluster and three iron atoms stand out clearly and can be used to locate these distinctive cofactors with confidence. The Mn cluster is located off the twofold axis of the heterodimeric protein complex at the luminal surface of the thylakoid membrane at the ends of the third and fifth transmembrane α -helices (“C” and “E”) of the D1 subunit. In the current model the closest electron density within the Mn cluster is located 7.0 Å from a protrusion in the electron density at the last turn of the C helix in D1 that is tentatively attributed to the side chain of Y_z .

No other density has been identified between Y_z and the Mn cluster. This assignment to Y_z is partially based on the presence of an equivalent protrusion of density assigned to tyrosine-D (Y_D) at the symmetry-related position in helix C of the D2 subunit. Y_D is present as a dark stable radical that is non-essential for water oxidation, although highly conserved in all PSII sequences.

Distance is critical for discriminating between the models used to describe how the Y_z radical oxidizes the Mn cluster. This distance of 7.0 Å refers to the length of a vector between the closest atomic positions modeled in the two cofactors, i.e. from Mn (or Ca) to the phenoxyl oxygen atom on Y_z . A hydrogen atom on a water molecule bound to the Mn cluster would be no closer than 4.5 Å to Y_z and possibly much farther. This distance is much too long to allow direct hydrogen atom transfer to the Y_z radical from a substrate water molecule bound to the Mn [16]. Because there is minimal structural change upon the first two S-state transitions [11], the hydrogen atom would have to fully dissociate or be carried by an unobserved diffusible H-atom carrier in order to move this distance. The activation energy of this pathway would be so great that we may eliminate it from consideration based on the known energetics [11]. However, mechanisms involving an obligatory base serving as a proton acceptor coupled to the electron transfer between the Mn cluster and Y_z are not precluded by the X-ray structural model [17, 18]. The structural data have not yet identified the location of this critical base, or for that matter, any of the peripheral atoms coordinated to the Mn cluster.

The dimensions of the electron density of the Mn cluster at the 5σ level are $6.8 \times 3.9 \times 3.3$ Å, with the long axis tilted about 23° against the membrane plane. There are three bulges in the electron density that define an isosceles triangle. However, the internal structure of the Mn cluster is not resolved with the present data, although the authors arbitrarily placed four Mn atoms within the density (Fig. 2a, b). It is not yet possible to distinguish between density arising from other expected heavy atoms such as calcium and chloride, both of which should contribute to the density considering the numerous other data supporting a close association of these cofactors with the Mn cluster. Anomalous diffraction data collected at a wavelength close to the Mn edge confirmed that Mn contributes to the global maximum of this electron density within a sphere of diameter 5 Å. Several possible geometries of four Mn atoms can be envisioned within this density. The two most probable Mn_4 -oxo core types that arise from consideration of the XAS and EPR data (see sections below) are drawn in Fig. 2c–e for comparison. The dimensions of both the $Mn_4O_4X_2$ funnel and the Mn_4O_2 butterfly core types suggest they would indeed fit within this border, but the volume is too large to accommodate these structures (as well as any other currently known tetramanganese-oxo/hydroxo core types) without additional unaccounted density. This may indicate space for Ca^{2+} and/or Cl^- . Until the data can be extended to higher resolution, the present model cannot provide unambiguous answers about the internal structure of the inorganic core of the WOC.

Fig. 2 **a** Electron density of the inorganic core of the WOC from the X-ray crystal structure of PSII. Approximate dimensions along each axis are shown [12]. **b** Electron density from **a** rotated 90° about the horizontal axis. **c** Molecular representation of the Mn_4 “funnel” structure that is proposed as a possible model for the tetranuclear Mn cluster of the WOC. Estimated dimensions along each axis are included. **d** Structure from **c** rotated 90° about the horizontal axis. **e** Molecular representation of the Mn_4 “butterfly” structure. Structures **c–e** are proposed on the basis of XAS and EPR studies



XAS of the WOC

XAS has proven to be a powerful probe of the structure and electronic properties of transition metal complexes and metalloenzymes [19, 20, 21]. X-ray absorption near edge spectroscopy (XANES) probes the core electron binding energy of the absorbing atom by exciting the electron into a higher energy bound state orbital. This energy depends on the oxidation state, coordination number, and ligand environment of the absorbing atom. Alternatively, extended X-ray absorption fine structure (EXAFS) spectroscopy ionizes the core electron, and the intensity of absorption or fluorescence is measured as the electron is backscattered by the surrounding nuclei. Thus, EXAFS is sensitive to the coordination number and ligand environment of the absorber. These techniques have been widely applied to the Mn cluster of the WOC, and many useful conclusions have been drawn. However, the oxidation states that have been derived for the Mn ions and the geometry and coordination structure of the cluster are not unanimously agreed upon. Moreover, these conclusions should be considered approximations since they have been deduced from empirical comparisons to a limited set of Mn model complexes that do not contain all of the atomic constituents of the enzyme (i.e. lacking Ca^{2+} , Cl^-). In this section we will critically evaluate the more speculative of these conclusions, and offer alternative interpretations that are consistent with both XAS and EPR data.

XANES

Oxidation state changes during the S-state cycle

The one-electron oxidation of manganese in model compounds leads to an increase in energy of the $\text{Mn}(1s \rightarrow 4p)$ K-edge by 1.6–2.0 eV in complexes exhibiting no major structural change [22]. This observation serves as the experimental basis for assigning changes in the Mn oxidation states of the WOC during S-state advancement based on changes in the Mn K-edge energy.

An increase in the Mn K-edge energy of 0.6–1.8 eV has been observed on both the S_0 – S_1 and S_1 – S_2 transitions (Fig. 3), which has been interpreted by all investigators as being consistent with oxidation of the manganese cluster [23, 24, 25]. However, there has been considerable disagreement as to whether or not a similar increase in the Mn K-edge energy accompanies the formation of the S_3 state. Ono et al. [24] and Iuzzolino et al. [25] observed a significant increase in the energy of the Mn K-edge (~ 1 eV) upon formation of S_3 from S_2 , which was interpreted in terms of Mn oxidation. In contrast, Roelofs et al. [23] observed only a 0.3 eV increase of the edge energy during this transition, which was interpreted as no net change in the Mn oxidation state, but rather oxidation of a coordinated His residue or a bridging oxo ligand [26].

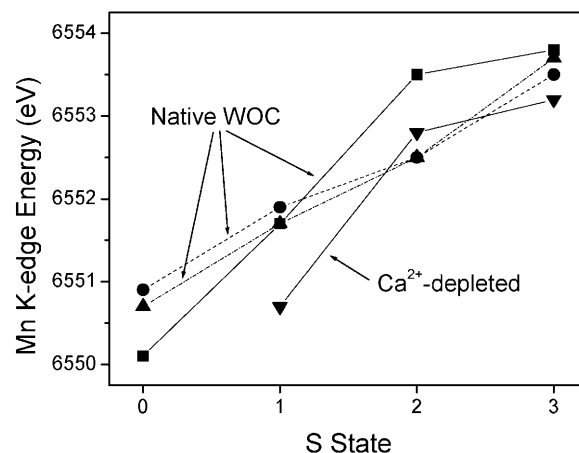


Fig. 3 Summary of the measured Mn K-edge energies for the S-states of the WOC as determined by independent investigators. Symbols: *triangles*, native WOC [23]; *squares*, native WOC [25]; *diamonds*, native WOC [24]; *inverted triangles*, Ca^{2+} -depleted WOC [39]

These studies have attempted to derive information about the Mn oxidation states from XANES spectra under the simplifying assumption that changes in the coordination environment of Mn are not contributing to the energy of the K-edge. However, Mn EXAFS has shown that a significant structural change occurs upon formation of the S_3 state from S_2 [26]. As we will discuss below, Mn-oxo complexes that exhibit the same formal oxidation state but different geometries or coordination numbers show large variations in the energy of the Mn K-edge. These results mean that we must look to other experiments for corroborating evidence for changes in the Mn oxidation state during S-state advancement in the WOC.

Determination of the average Mn oxidation state in each S-state

K-edge XANES. (1) Native WOC. EPR has shown that the S_1 state of the WOC is an integer-spin ground state (see section on EPR below). Hence, two possible oxidation states need to be considered for S_1 : $\text{Mn}_4(4\text{III})$ or $\text{Mn}_4(2\text{III},2\text{IV})$. XANES has been applied to discriminate between these two possibilities through comparison of the edge energies of the S-states (Fig. 3) to those observed for Mn-oxo model compounds [23, 27, 28]. On this basis, the oxidation states of the individual S-states were assigned as follows: S_0 (II,III,2IV or 3III,IV), S_1 (2III,2IV), S_2 (III,3IV), S_3 (III,3IV or 4IV). Others have agreed with these assignments based on their own Mn XANES studies, although using fewer Mn complexes for calibration [25, 29, 30].

A comparison of the published data for Mn-oxo model compounds [22, 23, 27, 31] reveals that the relationship between the Mn K-edge energy and Mn oxidation state is complex. The dependence of the Mn K-edge energy (defined by many as the inflection point

of the second derivative XANES spectrum) on the average Mn oxidation state in dinuclear, trinuclear, and tetranuclear Mn-oxo complexes is shown in Fig. 4. While a general correlation between Mn oxidation state and K-edge energy can be drawn within a set of complexes of the same cluster type, there are large differences between complexes of different nuclearities or cluster types. For example, $[\text{Mn}_3(\mu_3\text{-O})(\mu\text{-O}_2\text{CMe}_2)_6(\text{py})_3](\text{ClO}_4)$ (average Mn oxidation state = 3.0) and $\text{Mn}_4(\mu_3\text{-O})_3(\mu_3\text{-OMe})(\text{O}_2\text{CMe})_3(\text{dbm})_3$ (average Mn oxidation state = 3.25) exhibit higher Mn K-edge energies (6550.7 eV and 6551.3 eV, respectively) than $[\text{Mn}_2(\mu\text{-O})_2(\text{bpy})_4](\text{ClO}_4)_3$ (average Mn oxidation state = 3.5; Mn K-edge energy = 6549.9 eV). Even a series of complexes with the same Mn oxidation state and same overall structure can exhibit a large range of Mn K-edge energies. For example, the series of trigonally distorted cubane complexes $[\text{Mn}_4(\mu_3\text{-O})_3(\mu_3\text{-X})]^{6+}$ ($\text{X} = \text{OH}, \text{OMe}, \text{or } \text{O}_2\text{CR}$) exhibits a 1.2 eV range of Mn K-edge energies, even though these complexes all have an average Mn oxidation state of 3.25. If trigonally distorted cubanes that contain a bridging halide are included in this comparison, this range expands to 3.4 eV! From these examples it is clear that one cannot draw firm conclusions about the oxidation state of a manganese complex of unknown coordination number and geometry from the Mn K-edge energy alone. We will further discuss alternatives for the oxidation state assignment below.

(2) Ca^{2+} -depleted/substituted WOC. Ca^{2+} depletion of PSII leads to the complete but reversible inhibition of water oxidation activity [4, 32]. Replacement of Ca^{2+} with Sr^{2+} leads to partial restoration of activity [33, 34], while other metals such as La^{3+} and Dy^{3+} bind in the Ca^{2+} site with no stimulation of enzymatic activity [35]. Both Ca^{2+} depletion and substitution lead to altered EPR spectra from the Mn cluster [36, 37, 38]. The energy of the Mn K-edge decreases by 0.6–1.0 eV in each

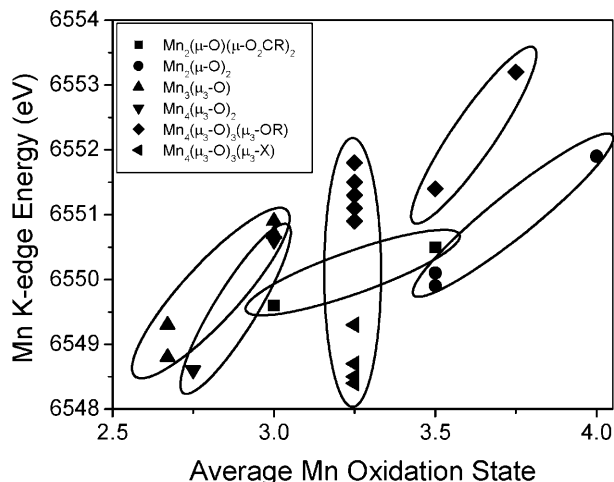


Fig. 4 Mn K-edge energies for Mn-oxo model compounds. The core types that have been considered are shown in the inset. Compounds with related structures are enclosed as a guide for the eye

S-state (S_1 , S_2 , and S_3) upon removal of the Ca^{2+} cofactor (Fig. 3) [39, 40, 41]. This effect is completely reversed upon addition of Ca^{2+} in the dark, consistent with no net reduction of the WOC upon Ca^{2+} removal. Replacement of Ca^{2+} with other cations (Sr^{2+} [42, 43], Dy^{3+} or La^{3+} [43]) results in a Mn K-edge that is similar in energy and overall shape to the native protein.

How does the Ca^{2+} cofactor alter the Mn K-edge position? The suggested causes were either reduction of manganese or an overall structural change. The first cause was ruled out as described above, since the normal Mn K-edge is reproduced upon reconstitution of the Ca^{2+} -depleted samples in the dark with Ca^{2+} , Dy^{3+} , or La^{3+} . A structural change has been hypothesized [39, 40, 41]; however, EXAFS shows that no large-scale structural changes in the manganese cluster accompany Ca^{2+} removal (see below) [39], which is further supported by the EPR data on S_2 (see section on EPR below). If the observed edge shift is later found to result from a minor coordination change around the manganese cluster, this provides another example to show just how sensitive the K-edge is to the Mn coordination environment, and not just the Mn oxidation state.

Another possible, and we believe likely, cause for the downshift in the Mn K-edge energy upon Ca^{2+} depletion involves a change in the covalency of the Mn-ligand bonds in the cluster [44]. If Ca^{2+} and the Mn cluster share one or more ligand (i.e. bridging ligand X), then removal of Ca^{2+} from the WOC would increase the electron density on Mn due to increased ligand-to-metal charge transfer (LMCT). Increased LMCT to Mn occurs primarily to the valence 3d and 4p orbitals on Mn and thus raises their energy relative to the core 1s orbital. As a result of increased electron repulsion, the K-edge transition energy ($1s \rightarrow 4p$) will noticeably increase. If, on the other hand, protonation of the bridging ligand accompanies Ca^{2+} depletion (XH^+), the LMCT to the Mn cluster would be substantially reduced and the K-edge shift should instead decrease in energy. This mechanism predicts that the same magnitude of shift in the Mn K-edge energy should be observed upon Ca^{2+} depletion for each S-state, in agreement with the data for S_1 , S_2 , and S_3 (Fig. 3). Although it is not known whether protonation of other ion compensation effects (such as release of Cl^-) occur upon removal of Ca^{2+} from the WOC, charge neutralization is normally the rule in biochemistry, and especially in membrane proteins like PSII.

To further illustrate this point, one can compare the gas phase ionization energy of CaO (6.66 eV), H_2O (12.62 eV), and atomic O (13.6 eV) [45]. Here one sees that the binding energy of an electron in the HOMO decreases by 7 eV (versus free atomic O) when Ca is bound to an O atom, compared to a 1 eV decrease if two H atoms are bound to the O. Thus, addition of Ca is expected to substantially increase the polarizability and thus availability of the O valence electrons for bonding to other atoms in a cluster (increase in Mn K-edge). Replacement of Ca by two H atoms almost completely

suppresses this effect. This argument means that the observed 0.6–1 eV decrease in the Mn K-edge upon depletion of the Ca^{2+} cofactor from the WOC is consistent with elementary considerations of shared bonding with a common set of ligand(s) that bridge between Ca and Mn in the WOC. Protonation of the shared ligands upon Ca^{2+} removal would account for the decrease in the Mn K-edge by this mechanism. In addition, Mn EXAFS and changes in Mn spin density distribution seen by EPR also indicate a close interaction and electronic coupling between Mn and Ca in the WOC (see below).

This interpretation of the Mn XANES data suggests a direct role for Ca^{2+} in facilitating the oxidation of the Mn cluster. Although the identity of the bridging ligands is unknown, it is evident that Ca^{2+} would play a direct role in substrate water activation if these bridges are substrate water ligands (see Fig. 9 below).

Mn K β fluorescence. An alternative method that is being developed is the study of the Mn K β emission line, which occurs at lower energies than the Mn K-edge, and is less sensitive to the ligand environment. The S_1 state of the WOC and some model compounds have recently been studied by K β fluorescence [46]. Correlation of the S_1 Mn K β energy in the WOC to model compounds has been interpreted as support for the formulation of S_1 as the mixed-valent $\text{Mn}_4(2\text{III},2\text{IV})$. However, this method produces a peak shift of only 0.65 eV between Mn(II) and Mn(IV) in the model compounds that were examined. This is a very small shift considering that the energies (~ 6490 eV) and peak widths ($\text{fwhm} \approx 4$ eV) are much larger than the energy differences between the complexes. It is non-trivial to measure these small differences with the precision necessary to draw meaningful conclusions from such a small set of model complexes, none of which constitute isostructural members of a redox series. At present, it is premature to state whether this technique can really be considered a better predictor of Mn oxidation states than traditional Mn K-edge XANES.

Structure of WOC based on EXAFS

Foundations of the EXAFS model

EXAFS has been the primary tool used to date for the determination of the interatomic distances of the WOC. The evidence for the proposed structural models derived from EXAFS has been reviewed in detail [28, 47], so we will focus only on the debated features.

EXAFS of the S_1 and S_2 states of the WOC show three peaks in the Fourier transformation of the k -space data at approximately 1.85, 2.74, and 3.31 Å [27, 48]. The first shell at 1.85 Å has been assigned to backscattering from the first coordination sphere of Mn, which is proposed to consist primarily of O-donor ligands,

although there is also evidence from EPR for one N-donor ligand from a His residue [49]. (EXAFS is not able to differentiate between C, O, and N.) There is agreement that the 2.74 Å shell arises exclusively from backscattering from Mn, implying that the WOC contains Mn-Mn separations of this distance. The third shell at 3.3 Å has been assigned primarily to backscattering from Mn and Ca [27, 48]. This interpretation is not universally accepted, as it has been proposed that light atoms (i.e. C) from the second coordination shell of Mn contribute to this peak [50]. The involvement of calcium in this shell has also been questioned (see below).

The number of scatterers at each distance was estimated by Fourier fitting of the k -space amplitudes. From these fits, a series of 10 structures that contain the predicted number of scatterers at the observed distances were proposed (see Fig. 5, structures 1–10) [48]. Of these structures, the “dimer-of-dimers” model (1) was selected to be the closest fit to the EXAFS results. This model consists of a pair of $\text{Mn}_2(\mu\text{-O})_2$ dimers linked using an $\text{Mn}_2(\mu\text{-O})(\mu\text{-O}_2\text{CR})_2$ unit. In model Mn-oxo complexes, the $\text{Mn}_2(\mu\text{-O})_2$ unit typically has Mn-Mn distances of approximately 2.7 Å, while the $\text{Mn}_2(\mu\text{-O})(\mu\text{-O}_2\text{CR})_2$ unit typically exhibits Mn-Mn distances of approximately 3.15 Å.

Some shortcomings of the proposed fits should be pointed out. The first Fourier peak at 1.85 Å was fit by only 2.0–2.5 O atoms. The rest of the first coordination shell was not well defined, and is likely disordered, and could only be modeled using high Debye-Waller factors. Since the first coordination shell is disordered, it is likely that the higher-order coordination shells are also disordered. Thus, the fits estimated previously for the second and third Fourier peaks should only serve as lower bounds for the number of heavy-atom scatterers at the observed distances, and not as the mean or best value. This flexibility will allow for a much larger library of structures that could potentially fit the EXAFS data.

The assignment of the 3.3 Å interaction to a $\text{Mn}_2(\mu\text{-O})(\mu\text{-O}_2\text{CR})_2$ unit is also open to debate, since this unit exhibits significantly shorter Mn-Mn separations, ranging from 3.08 to 3.23 Å, in all structurally characterized model compounds (see, for example, [51, 52, 53]). Importantly, the $\text{Mn}_2(\mu\text{-O})(\mu\text{-O}_2\text{CR})_2$ core is found almost exclusively at the $\text{Mn}_2(2\text{III})$ level, with only one example of a complex in the $\text{Mn}_2(\text{III,IV})$ level [54]. Oxidation of complexes with this core structure leads to a spontaneous structural rearrangement to the $\text{Mn}_2(\mu\text{-O})_2(\mu\text{-O}_2\text{CR})_2$ core, having a Mn-Mn separation of 2.7 Å [55]. Thus, the $\text{Mn}_2(\mu\text{-O})(\mu\text{-O}_2\text{CR})_2$ core type is not likely to be stable in the oxidation states proposed on the basis of Mn XANES, which assigns the S_2 state as $\text{Mn}_4(\text{III},3\text{IV})$ (see above). Hence, the oxidation state assignment from Mn XANES and the dimer-of-dimers structural model from EXAFS are incompatible with one another based on the interdependence of structure and oxidation state that has been demonstrated in model compounds. This analysis and the data from EPR (see

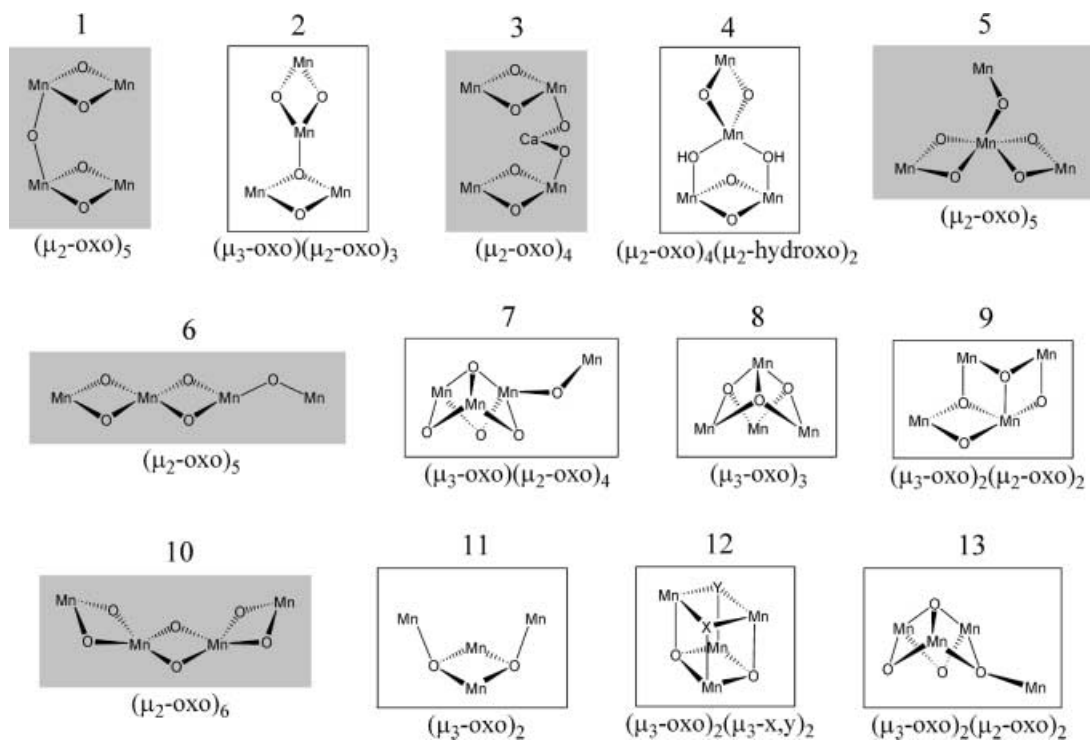


Fig. 5 Proposed structures of the Mn₄O_x cluster and bridging oxygen ligands of the WOC of PSII. Structures 1–10 were proposed on the basis of Mn EXAFS studies. The *shaded structures* are incompatible with the magnetic/electronic interactions derived from EPR data. *Unshaded structures* (2, 4, 7–9, 11–13) are compatible with both the Mn EXAFS and EPR data

below) refute both the dimer-of-dimers structural model and the XANES-derived Mn oxidation state proposal.

Location of Ca²⁺ with respect to the Mn cluster

Mn EXAFS has also been used to probe the proximity of the Ca²⁺ binding site to the Mn cluster by focusing on the contribution that Ca²⁺ has to the third Fourier peak at ~3.3 Å. However, these studies have generated conflicting interpretations. Latimer et al. [42] examined the Mn EXAFS of PSII samples in which Ca²⁺ is replaced with Sr²⁺. They observed an increase in the amplitude of the third Fourier peak, which the authors ascribed to the increased photoelectron backscattering cross section of Sr²⁺ relative to Ca²⁺, implying that Sr²⁺ contributes to the peak. The first two Fourier peaks were not affected by substitution at the Ca²⁺ site. In contrast, Riggs-Gelasco et al. [43] observed no such increase in the amplitude of the third Fourier peak in PSII samples in which Ca²⁺ was replaced by Sr²⁺, La³⁺, or Dy³⁺. Thus, they concluded that it was not possible to locate the position of the Ca²⁺ ion relative to the Mn cluster with this experiment.

More recently, Sr EXAFS was performed on PSII samples in which Ca²⁺ is replaced with Sr²⁺ [31]. This revealed a significant heavy-atom interaction at 3.6 Å,

which was interpreted as arising from backscattering from Mn. These data provide much more conclusive evidence that the Ca²⁺ site is in close proximity (3.4–3.6 Å) to the Mn cluster.

The structure of the Mn cluster upon Ca²⁺ depletion in PSII has also been examined by Mn EXAFS [39]. The most dramatic changes were observed in the modified S₁' state, in which all Fourier peaks were broader and smaller in amplitude than the corresponding peaks in native samples, indicating increased heterogeneity in the Mn-ligand and Mn-Mn distances. The higher modified S-states (S₂' and S₃') were more similar to their native S-state counterparts than in S₁'. The third Fourier peak exhibits a decrease in amplitude in all S-states, consistent with the removal of the Ca²⁺ contribution to this peak. It was concluded that removal of the Ca²⁺ cofactor does not greatly alter the primary structural features of the Mn cluster, but that a slightly larger range of Mn-ligand and Mn-Mn distances is present in Ca²⁺-depleted samples than in native samples.

Structural changes during S-state advancement

A majority of the EXAFS studies has been performed on the dark-stable S₁ state of the WOC [27, 48, 50]. These studies have served as the basis for the dimer-of-dimers structural model of the WOC described above, and all structural changes seen in the other S-states have been interpreted relative to this original model.

The S₂ state can be formed in high yield, and has been found to exhibit very similar Mn EXAFS spectra to the S₁ state [48, 56]. The native S₀ state is very difficult to

obtain in high yield and isolated from other S-states. However, spectra obtained on this state (formed by chemical reduction or by flashes) appear to show that the structure is similar to S_1 and S_2 [57, 58].

Recently, the S_3 state was studied in great detail by Mn EXAFS [26]. In this state the 2.74 Å vector assigned to Mn-Mn scattering lengthens and splits into two vectors at 2.8 and 3.0 Å. The 3.3 Å vector also lengthens and could be resolved as two vectors at 3.4 Å (assigned to Mn-Mn scattering) and 3.6 Å (assigned to Mn-Ca scattering), according to the fits for these peaks. The authors interpreted these changes as an increase in the intra-dimer distances, possibly resulting from the formation of a bridging oxyl radical, suggesting the one-electron oxidation of an oxide bridge rather than Mn. This proposal is consistent with the small XANES edge shift for the S_2 to S_3 transition (see above). However, oxyl radical formation has never been demonstrated in Mn-oxo model compounds.

The EXAFS interpretation of the S_3 state of the WOC does not follow the example of any known dimanganese model compounds and thus does not support the dimer-of-dimers structural proposal. Instead of proposing structural changes within dimers that have no precedence in the relevant Mn model compounds, consideration should be given to alternative Mn-oxo structure types that are consistent with the observed metrical data.

Structurally characterized tetramanganese core types that contain Mn-Mn and Mn-O distances that are compatible with those seen in the S-states of the WOC are the incomplete cubane (Fig. 5, structure **12**), $Mn_4(\mu_3-O)_3(\mu_3-X)$ ($X = OH, Cl, Br, O_2CR$) [59, 60, 61, 62, 63, 64], the planar butterfly (Fig. 5, structure **11**), $Mn_4(\mu_3-O)_2$ [65, 66, 67, 68], and the symmetric cubane, $Mn_4(\mu_3-O)_4$ [69, 70]. These clusters exhibit Mn-Mn distances that range from 2.8 to 3.3 Å. Recently, Cinco et al. [31] reported a comparison between model compounds having the distorted cubane topology and the WOC. This class of complexes was shown to reproduce the

location of all of the Fourier peaks observed in EXAFS of the S_1 and S_2 states of the WOC. However, the authors argued that they were not good models for the WOC on the basis that the Fourier amplitudes derived from the model compounds did not accurately reproduce those observed in the WOC. However, it was also observed in the model compounds examined in this study that the Fourier amplitudes exhibit large variations within the series of isostructural cubane complexes, thus demonstrating that the amplitude criteria alone cannot be used to exclude these core types from consideration for the structure of the Mn cluster of the WOC.

EPR and ENDOR spectroscopy of the WOC

Four of the five S-state intermediates have now been characterized by EPR, and also by ENDOR spectroscopy for the S_2 state. The first reports for the S_0 , S_1 , S_3 , and NO-reduced S_{-N} states became available in the last three years. This wealth of new information has provided considerable new insights. A recent review has summarized the EPR/ENDOR signals associated with the S_0 - S_2 and $S_2Y_z^\bullet$ states [71]. Table 1 lists the characteristics of the EPR signals reported to date. Herein, we focus on the proposed interpretations of the EPR parameters that provide constraints on the geometric structure and the electronic states of the Mn_4 cluster when referenced to model complexes.

S_2 state EPR/ENDOR

Experimental observations

The S_2 state has been extensively characterized by EPR (Table 1). Two distinct ground-state EPR signals have been assigned to the S_2 state: the “g2 multiline” signal centered at $g=2$ and split into 19–21 lines (85–90 G) attributed to ^{55}Mn hyperfine structure [2, 72] and the

Table 1 EPR data for the S-states

S-state	Spin state	Apparent g-factor (9 GHz)	^{55}Mn hyperfine (A = line splitting)	ΔE (cm $^{-1}$) ^a	Ref
S_0	$S = 1/2$ (ground)	2	≥ 20 lines ($A \approx 82$ G)	17–30 ^b	[127, 128]
S_1	$S = 1$ (low-lying excited)	4.8	None	1.7 ^c	[134, 135]
	$S = \text{integer}$ (ground or low-lying excited)	12	19–21 lines ($A = 32$ G)	< 2 ^c	[136, 137]
S_2	$S = 1/2$ (ground)	2 “multiline”	19–21 lines ($A = 89$ G)	36.5 ^b	[2]
	$S = 5/2$ (ground)	4.1–4.25 “g4”	> 16 lines, observable in oriented membranes	< 10 ^b	[73, 74, 83, 128, 151]
$S_2 + NH_3$	$S \geq 5/2$	10, 6	None	?	[76, 77]
	$S = 1/2$ (ground)	2 “multiline”	26 lines ($A = 67$ G)	33.5 ^b	[75, 152]
$S_2Y_z^\bullet$	Radical pair, $2 \times (S = 1/2)$	2	Similar to S_2 multiline	?	[36, 141, 142]
S_3	$S = 1$ (low-lying excited)	12, 8, 6.7	None	2.4 ^c	[139, 140]
S_{-N}	$S = 1/2$ (ground)	2	19 lines ($A \approx 80$ G)	29 ^b	[122]

^aTaken from [71, 76, 133, 135, 139, 153, 154] and Britt RD (personal communication)

^bEnergy gap from ground paramagnetic $S = 1/2$ or $5/2$ state to the first excited state

^cEnergy gap from ground diamagnetic $S = 0$ state to excited paramagnetic state

unstructured “*g4*” signal ($g = 4.1\text{--}4.25$) with a spectral width of 320–360 G [73, 74]. The *g4* signal also exhibits ^{55}Mn hyperfine structure (≥ 16 lines spaced by 36 G) that becomes resolved in oriented membranes, after treatment with NH_3 [75] or following near-IR illumination of Ca^{2+} -depleted samples [76].¹ A third featureless signal has also been reported situated at *g10* and *g6* that is produced by near-IR illumination of the S_2 “multiline” signal at 65 K and assigned to a thermally unrelaxed S_2 state with $S \geq 5/2$ [77]. The *g10* and *g6* S_2 signals relax to the *g4* form in the dark by increasing the temperature between 77 K and 140 K, while above 150 K the *g4* signal relaxes into the *g2* multiline form.

Variable-temperature EPR studies show that the S_2 multiline signal originates from an electronic ground state with spin $S = 1/2$ [78, 79, 80]. The S_2 *g4* signal formed by 140 K illumination has been attributed to a ground state with spin $S = 5/2$ on the basis of multifrequency EPR [81], pulsed-EPR spin nutation studies [82], and variable-temperature magnetic susceptibility studies [76, 83]. An alternative formulation of $S = 3/2$ based on fixed frequency (9 GHz), variable-temperature EPR experiments [84, 85] is no longer viewed as a likely alternative [76]. The same electronic state (with spin $S = 5/2$) appears to form in the S_2 *g4* state upon advancement of S_1 to S_2 by illumination of PSII at 140 K, or alternatively by near-IR illumination at 140 K of PSII initially in the *g2*-multiline S_2 state (which does not advance S -states). A near-IR absorption band associated with the Mn cluster in the S_2 and S_3 states has been identified and is the presumed excited state involved in the interconversion of the different ground-state forms of the S_2 state [86, 87].

The observation of the interconversion between the *g2* multiline and *g4* forms of the S_2 state is quite significant. It confirms that the two signals are associated with different electronic structures of the same Mn_4 cluster, differing in electronic ground spin (i.e. $S = 1/2$ and $S = 5/2$). Furthermore, since no major conformational change in the Mn_4 cluster is expected to occur at temperatures below 150–200 K, the interconversion indicates that the two forms must have quite similar geometric structures. No new bridging or terminal ligands to the Mn_4 cluster are expected to form (see table 2 in [88] and discussion). These states were suggested to have either distinct Mn charge distributions within the mixed-valence Mn_4 cluster, or a change in the local electronic ground-state configuration of a Mn(III) ion (e.g. the “hole” in the $3d^4$ configuration occupies a different *d* orbital).

Mn EXAFS studies have suggested a small structural change upon conversion of the *g2* multiline to the *g4* forms of the S_2 state. The change was interpreted to arise from a small increase (0.15 Å) in the one of the short (2.7 Å) inter-manganese separations, conjectured to be due to protonation of one oxo bridge [28, 89]. However,

no difference has been detected between the $\text{S}_2\text{--S}_1$ FTIR difference spectra (1000–1800 cm^{-1} region) prepared under similar conditions in which either the *g2* multiline or the *g4* forms of the S_2 state were populated [90]. Berthomieu and Boussac also found that Ca-depleted (chelator-treated)² PSII which forms the *g4* S_2 state did not produce an $\text{S}_2\text{--S}_1$ FTIR difference signal that differed from that found for the native *g2* multiline S_2 state (Berthomieu C, Boussac A, personal communication). In summary, EXAFS and FTIR data indicate that there is minimal or no observable change in the inner coordination structure of the Mn_4 cluster that accompanies the conversion between the low-spin *g2* and intermediate-spin *g4* electronic states of the S_2 cluster.

Native and NH₃-bound g2 multiline EPR signals

The large spectral breadth (> 1900 G) and spectral density of the ^{55}Mn hyperfine transitions (19–21 lines) that characterize the S_2 multiline EPR signal led to an early structural description based on comparison to model complexes [3, 91, 92] in which electron spin density is distributed on all four Mn ions in a single, spin-coupled, Mn_4 cluster in a ground or low-lying $S = 1/2$ state. The doublet-spin state requires an odd-electron count, with suggested Mn oxidation states of either (3III,IV) or (III,3IV). Isotropic EPR simulations further eliminated models based on a Mn trimer plus isolated Mn monomer geometry [93]. Subsequent unconstrained EPR spectral simulations led to an alternative interpretation of two isolated Mn dimers [94], that was argued to be unrealistic based on inexplicably large ^{55}Mn quadrupole parameters [95] and subsequently definitively refuted by ^{55}Mn ENDOR studies [96]. There now appears to be consensus on the tetra-nuclearity of the Mn cluster as a single electronically and magnetically coupled core in the S_2 state [3, 95, 96, 97, 98].

Further evidence identifying large electron spin density on all four Mn ions in the cluster has come from spectral simulations of the NH_3 -modified form of the *g2* multiline EPR signal in the S_2 state [95, 96]. This signal exhibits a 25% reduction of the mean hyperfine splitting from ^{55}Mn with no loss of spectral breadth, achieved by an increase in the number of lines from ~ 21 to ~ 26 (Table 1). Hence, the spin density redistributes among the Mn ions, rather than being transferred to other atoms.

ENDOR spectroscopy has given improved resolution of the observable ^{55}Mn hyperfine tensors and the first direct estimate of the ^{55}Mn quadrupole tensors [96]. Comparable (although not identical) spin density distributions among the four Mn ions have been derived from the ^{55}Mn hyperfine tensors obtained from simulations of the EPR spectra [95] and the EPR and ENDOR spectra [96]. In both the native and NH_3 -treated WOC,

¹Near-IR illumination refers to wavelengths ≥ 760 nm beyond the absorption region of the PSII pigments

²EGTA: ethylene glycol-bis(β -aminoethyl ether)-*N,N,N',N'*-tetraacetic acid

the spin density, measured from the isotropic part of the Mn hyperfine tensors (a_{iso}), reveals two Mn ions with nearly identical spin densities (differing by 9% a_{iso}). A second pair of Mn ions differs in magnitude from the first pair by 15–35% spin density and are inequivalent. Thus, the hyperfine data indicate a spin density distribution within the Mn_4 cluster that possesses approximate C_2 or C_s symmetry, suggesting either a two-fold axis or a reflection plane relating the individual Mn spin densities. This spin distribution reflects the electronic symmetry of the Mn_4 cluster in the S_2 state.

Two [95, 96] of the three [97] groups that have reported anisotropic simulations of both the native and NH_3 -treated multiline EPR spectra (9 GHz data only) now agree on the spin density distribution in the S_2 cluster. These groups use spin hamiltonians with different complexity and thus differ in the number of parameters. In the simulations by Peloquin et al. [96], ^{55}Mn ENDOR data were included to provide additional constraints for the EPR simulations, but the simulations also required eight additional fitting parameters in the spin hamiltonian. Are these simulations improved because they have additional data constraints, or are the additional fitting parameters required by the more complex spin hamiltonian producing the better spectral fits? Unfortunately, no measure of the co-variance of the derived parameters was provided by either of these groups. EPR data at other frequencies or other experimental approaches are needed to improve the reliability of the derived parameters.

There is one debated issue that has not yet been resolved. The physical origin of the anisotropic part of the derived ^{55}Mn hyperfine tensors is debated. Peloquin et al. [96] assign the hyperfine anisotropy observed in the g_2 multiline spectra to the effect of zero-field splitting at Mn(III), a result that requires admixture of high spin states ($S > 1/2$) into the ground state. Small energy gaps to the excited states relative to the zero-field splitting are required for this mechanism to contribute. By contrast, Zheng et al. [99] assign the hyperfine anisotropy observed in the S_2 spectra to the classical magnetic dipolar interaction in a pure doublet-spin state ($S = 1/2$), arising from the non-spherical spin density on each Mn ion, primarily Mn(III). It is difficult at present to determine how much of each of these different mechanisms contributes. The attribution of the hyperfine anisotropy to different physical mechanisms has led to two different proposals for the Mn oxidation states, $\text{Mn}_4(3\text{III}, 1\text{IV})$ [95] and $\text{Mn}_4(1\text{III}, 3\text{IV})$ [96]. The lack of clarification in the origin of the hyperfine anisotropy makes it difficult to decide between the two possible Mn oxidation state models proposed for S_2 , as it hinges directly upon the physical mechanism that produces the anisotropy. Because it is unclear which mechanism dominates, both oxidation state proposals ought to be considered as candidates based on the ^{55}Mn hyperfine data that are currently available.

We stress that the assignment of S_2 to the oxidation state $\text{Mn}_4(3\text{III}, 1\text{IV})$, based on the ^{55}Mn hyperfine data, is

also consistent with the oxidation assignment we presented in the XAS section (above) based on the Mn K-edge energies of *Ca-depleted* samples. Thus, the lower oxidation state proposed for S_2 is consistent with two independent lines of evidence and thus provides the most consistent interpretation of all of the data at hand.

EPR detection of Ca^{2+} interaction with the Mn_4 cluster

The g_2 multiline signal in the native S_2 state changes appreciably upon removal of Ca^{2+} [36, 37, 100]. There is a reduction in the spectral density of ^{55}Mn hyperfine transitions without much change in the overall spectral breadth. These changes are reversed upon reconstitution of Ca^{2+} . The observed changes suggest that there has been a decrease in the spin density on one or more of the Mn ions but no change in the spin state ($S = 1/2$). No satisfactory spectral simulation of this signal has been reported.

In vitro studies of the biogenesis of the inorganic core of the WOC from the free inorganic ions have shown that a Ca^{2+} ion binds to the apo-WOC-PSII protein (depleted of Mn and Ca) during reconstitution of O_2 evolution activity [101]. One Ca^{2+} ion was found to bind after the first Mn^{2+} was photo-oxidized. Uptake of this Ca^{2+} was coupled to an increase in the affinity or photo-oxidizability of the remaining three Mn^{2+} ions [102]. When similar experiments were done in the dark at elevated Mn^{2+} concentrations, prior binding of Ca^{2+} to apo-WOC-PSII was found to induce the co-binding of Mn^{2+} ions from solution. The Mn^{2+} ions that bound to apo-WOC-PSII formed a spin-coupled dimanganese(II,II) center that was also capable of photoactivation of O_2 evolution [103]. This effect was not observed when Mg^{2+} replaced Ca^{2+} . These data indicate that Ca^{2+} is specifically involved in formation of the binding site for the Mn ions and fostering electronic coupling between the Mn ions.

From these data and the effects of Ca^{2+} depletion on both the EPR of the Mn_4 cluster and the Mn XAS data, it can be confidently concluded that Ca^{2+} is intimately involved in determining the electronic and metrical structure of the Mn_4 cluster. It decreases the binding energy of Mn electrons by promoting LMCT, modulates the inter-manganese exchange coupling, and mediates the photo-oxidation of Mn ions by the Y_2 radical during turnover of PSII.

Magnetic coupling models for the Mn_4 cluster in the S_2 state

The foregoing data reveal that the g_2 multiline ($S = 1/2$) and g_4 ($S = 5/2$) spectral forms of the S_2 oxidation state do not differ appreciably in terms of the inner coordination sphere. This constraint places strong limitations on the allowed bridging ligand topology of the Mn_4 cluster. In order to produce electronic flexibility within a

structurally inflexible core requires the existence of multiple ligand bridges between the Mn ions. The electronic exchange interactions must be of comparable strength in order to compete for orienting the electronic spins on Mn. This phenomenon, known as “spin frustration,” produces a number of states very close in energy. An M_3 triangle geometry provides the simplest example of spin frustration, as it is impossible for all three pairs to have anti-parallel spins. This requirement for electronic flexibility argues strongly against geometries involving any linear, bent, or C-shaped Mn_4 chain. These geometries have only nearest-neighbor intermanganese interactions that create isolated ground states exclusively, with no option for changing the ground spin state without a major structural change. Independent evidence in support of this conclusion also comes from the detection of large spin density on each of the four Mn ions in the S_2 multiline state. This requires inter-manganese couplings that effectively compete for orientation of the electronic spins. The resulting electronic “spin frustration” produces the lowest possible total-spin ground state (for antiferromagnetic J_{ij}), but is constructed from Mn spin angular momentum states having the largest possible spin projection from each of the Mn ions.

The spin-projection method (also known as the vector-coupling method) has a firm theoretical basis and has been widely successful in the prediction of the electronic states of clusters having localized spins that are coupled by two-center spin-exchange interactions [104]. We and others have applied it extensively to the Mn_4 cluster of the WOC [92, 95, 96, 97, 105, 106]. Herein, we use this approach to evaluate all of the possible magneto-structural models as candidates for the Mn_4 cluster. In Fig. 5 we list the six possible electronic coupling models for a cluster comprising four Mn ions. Next, we rank each of these magnetic models in terms of their ability to account for the following five experimental observations:

1. Low-spin ($S=1/2$) ground states for both the native and NH_3 -bound S_2 multiline signals.
2. An energy gap of 37 and 33 cm^{-1} , respectively, to the first-excited state in these forms of the S_2 state.
3. Large electron spin densities on each of the four Mn ions with approximate C_2 or C_s symmetry of the spin density distribution over the Mn_4 cluster.
4. Isostructural interconversion between a low-spin, $S=1/2$, state (g_2 multiline signal) and an intermediate-spin, $S=5/2$, state (g_4 signal) by a local change in the inter-manganese coupling constants. Specifically, we allow no new ligand bridges (and thus no new exchange pathways) between Mn ions upon this interconversion. A protonation change of an oxo/hydroxo bridge is not precluded.
5. Population of an intermediate or higher spin state, $S=5/2$, of the S_2 state Mn_4 cluster responsible for the g_6/g_{10} signals, by a local change in one of the inter-manganese coupling constants.

To these we add a sixth empirical constraint that enables a structural model to be deduced:

6. All pair-wise exchange couplings (J_{ij}) within both mono- and di- μ -oxo-bridged $Mn_2(IV,IV)$ and $Mn_2(IV,III)$ pairs are taken to be strongly anti-ferromagnetic.

The last constraint has been confirmed experimentally (Table 2). Anti-ferromagnetic couplings in the range -87 to -440 cm^{-1} (mean J values) have been reported for numerous examples of di- μ -oxo-bridged Mn_2 complexes containing any combination of Mn(III) and Mn(IV) ions as well as with or without carboxylate bridges [107, 108, 109]. However, the coupling becomes much weaker or zero and in some cases changes sign to weakly ferromagnetic within mono- μ -oxo-bridged $Mn_2(III,III)$ pairs [99, 109, 110, 111]. A weakly coupled ferromagnetic $Mn_2(IV,IV)$ pair ($J=+10$ cm^{-1}) has also been reported in this core type, but with non-physiological di- μ -borate bridges [112]. Hydroxo-bridged Mn ions have much weaker anti-ferromagnetic couplings in the range of -10 cm^{-1} . Triply bridging (μ_3)-oxo atoms, which adopt the planar M_3O geometry, provide bridging pathways among three Mn ions that have moderate anti-ferromagnetic couplings similar in magnitude to hydroxo bridges [107, 113]. Anti-ferromagnetic coupling increases when the π -bonding overlap of the oxygen $2p_\pi$ and manganese $3d_\pi$ orbitals increases, and thus is a good indicator of stronger Mn-O bonding.

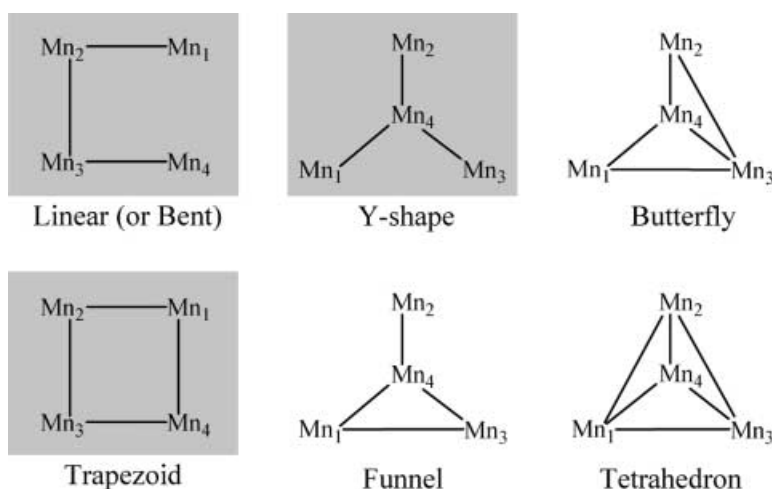
Linear/bent Mn_4 core

In the linear, bent, or C-shaped models (Fig. 6), three of the six possible exchange couplings (J_{13} , J_{24} , J_{14} corresponding to next-nearest neighbor Mn ions) are zero, i.e. there are no bridges between the respective ions, and the nearest-neighbor couplings are all anti-ferromagnetic (J_{12} , J_{23} , $J_{34} < 0$). With any set of anti-ferromagnetic couplings, the linear cluster *always* has a ground $S=1/2$ state and is never in an intermediate- or high-spin ground state. Because of constraint 4, there can be no new bridges (exchange pathways) created in the cluster upon conversion from the g_2 multiline to the g_4 form. Therefore, the only way to achieve the conversion is to make one of the existing pathways (J_{12} or J_{34}) ferromagnetic in the g_4 form. In that case, the ground state would be $S=7/2$ or $9/2$ for a $Mn_4(3III,IV)$ cluster and

Table 2 Mean electron spin exchange coupling constants for oxo-bridged manganese complexes, as obtained from [107, 108, 109]

Structure type (Mn oxidation state)	J (cm^{-1})
$Mn_2(\mu-O)_2^{2+}$ (III,III)	-173 to -201
$Mn_2(\mu-O)_2^{2+}$ (III,IV)	-237 to -320
$Mn_2(\mu-O)_2(\mu-O_2CR)^{2+}$ (III,IV)	-228 to -440
$Mn_2(\mu-O)_2^{2+}$ (IV,IV)	-156 to -294
$Mn_2(\mu-O)_2(\mu-O_2CR)^{2+}$ (IV,IV)	-87 to -248

Fig. 6 Spin-coupling models for a Mn_4 cluster. The lines indicate an exchange-coupling path (J_{ij}) between Mn_i and Mn_j , which structurally corresponds to a ligand bridging between the Mn ions. Shaded structures are not acceptable magnetic models for the Mn_4 WOC



$S = 5/2$ or $7/2$ for a $Mn_4(III,3IV)$ cluster, depending on whether the unique $Mn(IV/III)$ is in a terminal or central position. Thus, a linear $Mn_4(3III,IV)$ cluster is ruled out as incapable of producing an intermediate-spin $S = 5/2$ state that is needed to account for the g_4 Mn_4 cluster.

In principle, the $Mn_4(III,3IV)$ oxidation state could produce a ground $S = 5/2$ state within a linear model, but would require ferromagnetic J_{12} (or J_{34}) coupling between two $Mn(IV)$ ions. Peloquin et al. [96] adopted this assumption in their linear “dangler” model of the Mn_4 cluster (identical to structure 6 in Fig. 5). They modeled the g_4 signal with a single μ_2 -oxo bridge between the dangler $Mn(IV)$ to the adjacent $Mn(IV)$ ion, assuming ferromagnetic exchange coupling. However, ferromagnetic coupling has been identified in only a single example of an $Mn_2(IV,IV)$ pair that is oxo bridged. This complex has a mono- μ_2 -oxo bridge and two non-physiological borate bridges that create ferromagnetic coupling through the borate π^* orbital [112]. Three-center bonding by B atoms is likely responsible for this unusual coupling. On the other hand, oxo bridges produce strong anti-ferromagnetic coupling between $Mn(IV)$ ions owing to the dominant π exchange pathway between the $Mn(IV)$ π -type t_2 electrons and the filled π -type 2p orbitals of the oxo bridge [108, 114]. Thus, the linear dangler model does not meet constraints 4 and 6, and is unlikely as a core type for the S_2 WOC.

Other authors have also argued against the linear or bent model based on constraints 1–3. Hasegawa et al. [115] have theoretically tested $Mn_4(III,3IV)$ cluster models and concluded that at least one additional anti-ferromagnetic pathway is required (in our notation, J_{24} or J_{13}), thus making it a “funnel” structure (compare Fig. 6). Belinskii [116] has analyzed both $Mn_4(3III,IV)$ and $Mn_4(III,3IV)$ cluster models and concluded that a linear model fails to describe the g_2 multiline signal using any reasonable set of J couplings and typical intrinsic hyperfine couplings on $Mn(III/IV)$ ions. The Berkeley dimer-of-dimers structural model in Fig. 5 (structure 1) is a subset of the linear/bent model and thus

is incompatible with the EPR data for S_2 [95, 96, 108, 117].

To date, only two Mn_4 complexes have been reported to exhibit a doublet-spin ground state and an EPR spectrum that is similar to the g_2 multiline S_2 signal. One of these has a linear core, $Mn(IV)-(\mu-O)_2-Mn(IV)-(\mu-O)_2-Mn(IV)-(\mu-O)_2-Mn(III)$. The EPR spectrum has a larger number of resolved lines (26 versus 19–21 for S_2) but has a comparable overall spectral breadth (1900 G) [106]. The EPR spectrum has been simulated using a linear exchange model with two terminal couplings, J_{12} and J_{34} , that are strongly anti-ferromagnetic. It was theoretically demonstrated that the third coupling (J_{23}) must also be strong (!), either anti- or ferro-magnetic, and comparable in magnitude to both J_{12} and J_{34} in order to create significant spin density on all four Mn ions (constraint 3). However, because all three J couplings are strong, the linear Mn_4O_6 complex possesses an isolated $S = 1/2$ ground state (ΔE is larger than 100 cm^{-1}). This is evident from the fact that EPR spectrum can be readily detected at temperatures well above 30 K [106]. Thus, constraints 2 and 3 impose opposite requirements to J couplings in linear complexes: all strong J couplings are required to meet constraint 3, while at least one weak J coupling is required to meet constraint 2, i.e. $\Delta E = 33\text{--}37\text{ cm}^{-1}$. Another serious shortcoming of the linear Mn_4O_6 model complex is the inability to form intermediate-spin or high-spin ground states (constraint 4) without major structural distortion.

Trapezoidal Mn_4 model

The trapezoid model in Fig. 6 can also be ruled out using similar reasoning as for the linear models. The presence of four anti-ferromagnetic pairwise couplings favors a low-spin ground state (absence of spin frustration). Inclusion of at least one strong (!) ferromagnetic coupling was also required to increase the spin density on four Mn ions (see fig. 5 in [116]), but led to an

isolated high-spin ground state that is not consistent with the $S=1/2$ of the g_2 multiline signal.

“Y-shaped” Mn_4 model

Another model that can be eliminated is the “Y-shaped” cluster in Fig. 6. With all J couplings anti-ferromagnetic ($J_{14}, J_{24}, J_{34} < 0$), the Y-shaped model invariably exhibits an intermediate-spin ground state, $S \geq 7/2$ for Mn_4 (3III,IV) and $S \geq 5/2$ for Mn_4 (III,3IV), and never exhibits a ground $S=1/2$ state. To obtain a ground $S=1/2$ state, one ferromagnetic coupling (J_{34}) needs to be assumed [96]. Alternatively, inclusion of an additional strong-to-moderate anti-ferromagnetic pathway in the cluster (for example, J_{13}) would create a ground $S=1/2$ state [117]. However, this model is already a “funnel” structure (see below). By analyzing the hyperfine structure of the g_2 multiline signal, Belinskii has stated (but not yet explicitly proved) that the Y-shaped model cannot describe the hyperfine structure, even assuming ferromagnetic J couplings [115, 116].

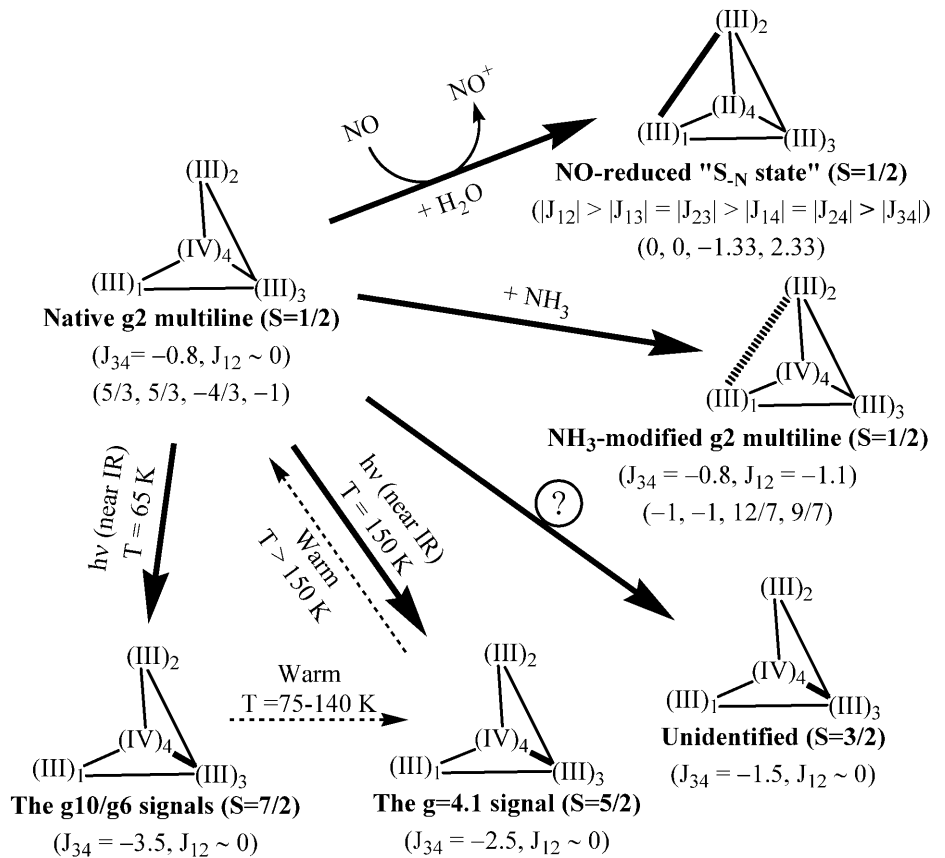
Funnel, butterfly, and tetrahedron models

The final three magnetic models in Fig. 6 (funnel, butterfly, and tetrahedron) have been previously investigated [95, 115, 116, 117]. We find that all three models are capable of satisfying all five constraints on

the EPR data noted above. Moreover, with each of these models the EPR constraints can be achieved using anti-ferromagnetic couplings, thus avoiding use of unprecedented ferromagnetic couplings for oxo-bridged Mn_2 (III,IV) pairs. All three models minimally contain a “triangle” motif, with each Mn ion coupled to two others in a triangle. This geometry provides the simplest example of spin frustration, as it is impossible for all three pairs in a triangle to have anti-parallel spins.

We illustrate in Fig. 7 the magnetic ground states predicted by the distorted tetrahedral magnetic model ($J_{13} \approx J_{14} \approx J_{23} \approx J_{24} \equiv J \equiv$ base-wingtip exchange). The oxidation state Mn_4 (3III,IV) will be considered, with the unique Mn(IV) at base position 4. A very similar analysis can be made assuming the oxidation state Mn_4 (III,3IV). Without loss of generality, we assume $J = -1$ (arbitrary units). For a butterfly model, taking $J_{12} = 0$ (wingtip-wingtip) and $J_{34} = -0.8$ (base-base), one obtains a ground $S=1/2$ state with a spin density distribution on all four Mn ions that was previously demonstrated to give an excellent simulation of the native S_2 multiline signal [95]. Adding the wingtip-wingtip coupling $J_{12} = -1.1$ gives a tetrahedron model, and a new $S=1/2$ state becomes the ground state. This state has a different distribution of spin density within the Mn_4 cluster that correctly describes the NH_3 -modified multiline signal. We previously emphasized that a single set of intrinsic ^{55}Mn hyperfine parameters reproduces both the native and NH_3 -bound g_2 multiline EPR signals, without the

Fig. 7 The diversity of S_2 -state EPR signals and their proposed attribution to distorted tetrahedral Mn_4 cluster model ($J_{13} \approx J_{14} \approx J_{23} \approx J_{24} \equiv J \equiv -1$). The varied J_{12} and J_{34} couplings and resulting ground spins (S) are designated for each structure. The spin density on each Mn ion is also listed for the $S=1/2$ ground state in sequence (Mn₁, Mn₂, Mn₃, Mn₄). High symmetry is not required. The allowed range of J_{ij} values that produces the same ground state has been examined in more detail elsewhere (see [95] for Mn tetramers and [106] for Mn dimers)



need for independent fitting of the parameter sets [95]. Only the electronic origin of the new doublet ground state changes because J_{12} controls the projection of the individual Mn spin angular momenta within the new ground electronic state.

This observed equivalence of the intrinsic ^{55}Mn hyperfine tensors (scalar traces) for the native and NH_3 -bound S_2 states is precisely the expected outcome if ammonia binding were to occur by ligand substitution at a bridging site between a pair of Mn ions, as suggested in Figs. 7 and 8. A bridging location for NH_3 was also concluded from the $^{14}\text{N}/^{15}\text{N}$ hyperfine and quadrupole parameters of the ammonia ligand from simulation of pulsed EPR data [118]. Keeping instead $J_{12}=0$ and allowing J_{34} to increase to -1.5 and then to -2.5 and -3.5 (butterfly model with varying “base” coupling), one obtains ground states with $S=3/2$, $5/2$, and $7/2$, respectively. Thus, the distorted tetrahedral magnetic model in Fig. 7 exhibits the essential flexibility needed to account for all four of the S_2 EPR signals, including the g_{10}/g_6 signals corresponding to the highest observed spin $S \geq 5/2$ and the g_4 signal assigned to an $S=5/2$ state. Moreover, this interconversion of states is achieved while preserving both the C_2 (C_s) symmetry of the Mn spin density and without invoking unprecedented ferromagnetic couplings between oxo-bridged Mn(III)Mn(IV) ions. Similar arguments hold for the “funnel” magnetic model (Fig. 8). We describe how to map these magnetic models onto chemically reasonable structures in the next section.

S_2 state Mn_4O_x chemical structures

In Fig. 5 (unshaded structures) we summarize the chemical structures for the Mn_4O_x cores that are con-

sistent with both the EPR data (constraints 1–5) and the more flexible interpretation of the Mn EXAFS data given in the XAS section (above). Structures **1**, **3**, **6**, and **10** are linear magnetic models, structures **2**, **4**, and **7** correspond to “funnel” magnetic models, **9**, **11**, and **13** to “butterfly” models, and **8** and **12** to “tetrahedron” models. Models **2**, **4**, **7**, **8**, and **9** have been put forward on the basis of previous Mn EXAFS results, while models **11**, **12**, and **13** were designated as inconsistent based on the relative peak intensities and the dichroism of the Mn EXAFS spectra [28, 31, 47, 48]. However, in the XAS section we disputed this interpretation in favor of a more conservative interpretation of the Mn EXAFS data that does not exclude models **11**, **12**, and **13**.

$\text{Mn}_4\text{O}_4(\text{X})_2$ funnel core

The $\text{Mn}_4\text{O}_4(\text{OH})_2$ funnel core structure **4** is one of two particularly well-suited core types that account for all aspects of the Mn EXAFS and EPR data in multiple S-states. There are no reported model complexes with this particular core type that we are aware of; thus we can only predict its magnetic properties. The Mn_3O_4 triangular subcore that comprises the base of **4** is widely represented in model complexes, with $[\text{Mn}_3\text{O}_4(\text{bpy})_4(\text{H}_2\text{O})_2]^{4+}$ and $[\text{Mn}_3\text{O}_4(\text{phen})_4(\text{H}_2\text{O})_2]^{4+}$ as representative examples [119, 120]. Their magnetic properties indicate a low-spin ground state ($S=1/2$) that is close in energy to a low-lying intermediate-spin state ($S=3/2$) [121]. This spin state ordering and small energy gap indicate the presence of spin frustration in the triangular core. Spin frustration gives rise to large spin density on all three Mn ions which is seen experimentally in the large magnitude of the ^{55}Mn hyperfine coupling constants that are comparable to those of the isolated ions

Fig. 8 Possible structural assignments of the S_2 EPR signals predicted by the “funnel” Mn_4O_6 model. The bridging ligand between Mn_2 and Mn_3 and the corresponding J_{23} coupling (indicated for each structure) are the only variables changing between the structures; the other bridges and couplings ($J_{12}=-3$, $J_{24}=-0.8$, $J_{34}=-0.4$) are kept constant. “B” indicates a base. The energy gap to the first excited state, $\Delta E = E(S=3/2) - E(\text{ground state})$, is calculated for each structure. Spin densities on four Mn ions are listed for the $S=1/2$ ground states in sequence (Mn₁, Mn₂, Mn₃, Mn₄)

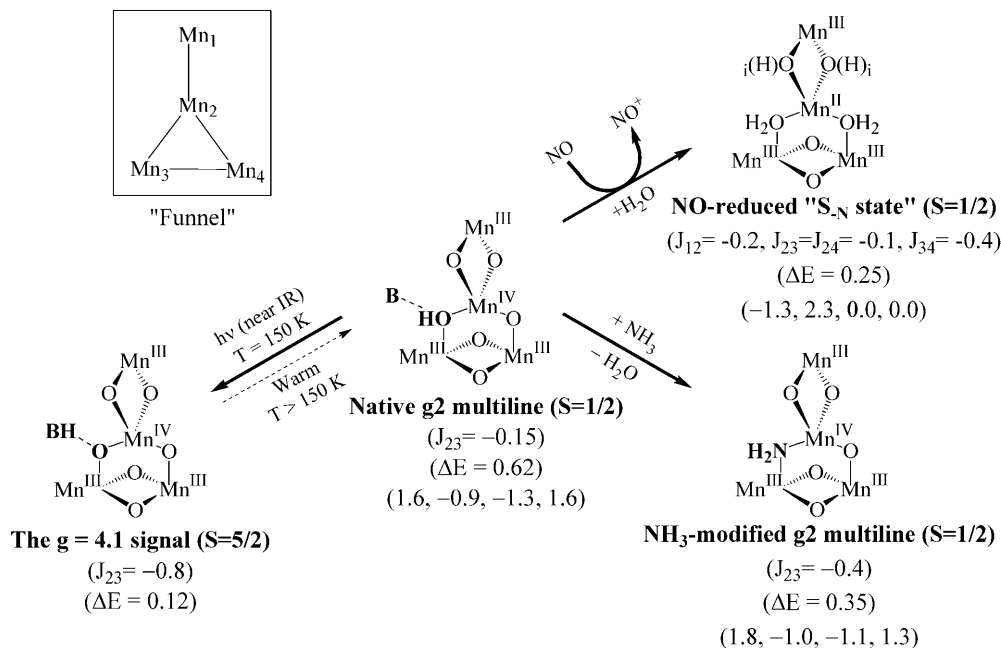
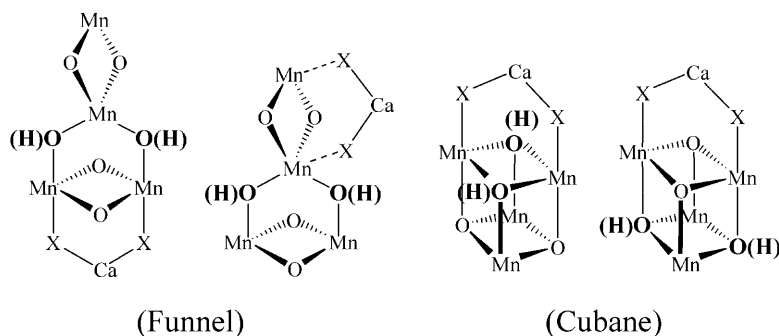


Fig. 9 Proposed location of Ca^{2+} relative to Mn within the two most favored Mn_4 core structures. *Boldface symbols* indicate the location of labile ligand sites that are leading candidates for the substrate water sites. $\text{X}^- = \text{Cl}^-$, OH^- , $^-\text{O}_2\text{CR}$, or HCO_3^-



[119]. By contrast, the linear Mn_3O_4 core is unsuitable as it exhibits an intermediate-spin state ($S=3/2$) as the ground state that is well isolated from excited spin states due to strong anti-ferromagnetic coupling and the absence of spin frustration.

Calculations show that the Mn_4O_6 funnel core will have a low-spin ($S=1/2$) ground state for both the $\text{Mn}_4(3\text{III},4\text{IV})$ and $\text{Mn}_4(3\text{III},3\text{IV})$ oxidation states, as summarized in Fig. 8. We used the $\text{Mn}_4(3\text{III},4\text{IV})$ core with unique $\text{Mn}(\text{IV})$ at the central position. A systematic search was undertaken of the spin exchange coupling network within a Mn_4 funnel core to satisfy both the large spin density distribution on Mn and predict the correct spin states for the three ground-state S_2 EPR signals. With the three couplings kept constant ($J_{12}=-3$, $J_{24}=-0.8$, $J_{34}=-0.4$, arbitrary units) and with only variable J_{23} , we were able to predict all three EPR signals. A low-spin ground state ($S=1/2$) with large spin densities on the four Mn ions (-1.3 , 1.61 , 1.66 , -0.97 ; note these fractional densities sum to 1.00) consistent with the native g_2 multiline signal was obtained with $J_{23}=-0.15$. This coupling model corresponds to asymmetric bridging in the funnel core ($J_{23} \neq J_{24}$). An intermediate-spin ground state ($S=5/2$) corresponding to the g_4 signal was obtained assuming a symmetric funnel core with $J_{23}=J_{24}=-0.8$. We suggest that the low-temperature interconversion of the g_2 multiline to the g_4 signal may correspond to a change in the hydrogen bonding of a hydroxo bridge by partial transfer to a neighboring base (base B in the asymmetric funnel core of the Mn_4 cluster in Fig. 8). As noted above, partial or complete loss of a proton from a hydroxo bridge is known to strengthen the inter-manganese exchange coupling (J_{23}).

Figure 8 shows that a different spin $S=1/2$ state is predicted to be the ground state using a J_{23} coupling that is intermediate in magnitude between that which produces the g_4 and native g_2 multiline signals. With $J_{23}=-0.4$ this new doublet spin state [there are a total of eight doublet states for $\text{Mn}_4(3\text{III},4\text{IV})$] possesses a different spin density distribution on Mn (-1.1 , 1.29 , 1.77 , -0.96) that correctly predicts the altered EPR spectrum of the NH_3 -bound g_2 multiline signal [95]. A bridging location and speciation as the amide (NH_2^-) have been previously proposed for the ammonia ligand based on its ^{14}N quadrupole tensor [118]. The present analysis is consis-

tent with this assignment. An increase in the J_{23} anti-ferromagnetic exchange coupling would be expected upon replacement of an OH^- bridge by an NH_2^- bridge in the Mn_4 cluster (Fig. 8).

In these calculations on the funnel models, the magnitudes of the exchange couplings needed to produce these states correlate well with the expected oxo-bridging topology given in Fig. 8. For example, the strongest coupling, $J_{12}=-3$, is predicted for the $\text{Mn}_2(\text{III},4\text{IV})$ pair that is bridged by two μ -oxo atoms, the moderate couplings, $J_{24}=-0.8$ and $J_{34}=-0.4$, correspond to the $\text{Mn}_2(\text{III},4\text{IV})$ pair with one μ -oxo bridge and the $\text{Mn}_2(\text{III},\text{III})$ pair with two μ -oxo bridges, respectively. The smallest coupling, $J_{23}=-0.15$, corresponds to the $\text{Mn}_2(\text{III},4\text{IV})$ pair with one μ -hydroxo bridge.

The energy gap to the first excited state was also calculated for each of the funnel models in Fig. 8. For all three structures in Fig. 8 the first excited state has spin $S=3/2$, and the energy gap is predicted to be $\Delta E=0.62$, 0.12 , and 0.35 (arbitrary units) for the native g_2 multiline, the g_4 , and the NH_3 -bound g_2 multiline clusters, respectively. These magnitudes correlate well with the experimental values of $\Delta E=37$, $\Delta E < 10$, and $\Delta E=33 \text{ cm}^{-1}$ for the respective S_2 clusters (Table 1).

A further critical test of the correct magnetic model is that it must also account for the well-resolved ^{55}Mn hyperfine structure from the EPR signal formed by reversible reduction of the S_1 state with excess NO gas [122]. This signal was attributed to an unknown oxidation state at or below the S_{-1} state and almost exactly matches the characteristic structure from simple dimeric $\text{Mn}_2(\text{II},\text{III})$ clusters [99]. Sarrou et al. [122] suggested that the Mn ions in this state might be magnetically decoupled into two isolated Mn_2 pairs, with one pair producing the $\text{Mn}_2(\text{II},\text{III})$ dimer-like signal and the second pair being EPR silent (i.e. with no hyperfine spin density) and thus either $\text{Mn}_2(\text{III},\text{III})$ or $\text{Mn}_2(\text{II},\text{II})$. Here, we asked if the intact (magnetically coupled) funnel core $\text{Mn}_4(\text{II},3\text{III})$ is also capable of explaining the appearance of the dimer EPR signal. We found that a wide range of couplings in a *symmetric* funnel core [with unique $\text{Mn}(\text{II})$ at central position 2] produces a ground $S=1/2$ state with the required spin density distribution (-1.33 , 2.33 , 0.0 , 0.0), i.e., with no spin density on two Mn ions and a spin distribution on the remaining two Mn ions

that exactly matches the $\text{Mn}_2(\text{II,III})$ dimer (Fig. 8, top right). This spin density distribution results from spin frustration within the triangular core of the funnel model ($J_{12} = -0.2$, $J_{23} = J_{24} = -0.1$, $J_{34} = -0.4$, $J_{13} = J_{14} = 0$). Each J_{ik} can be individually varied by 50% and still produce the same ground state $S = 1/2$ and the same spin density distribution. We found, however, that the C_{2v} (magnetic) symmetry of the core (i.e. $J_{23} = J_{24}$) is absolutely required and even a small 10% deviation of the symmetry results in significant spin density (± 0.5) on the two “silent” Mn ions. This symmetry requirement disappears when the coupling of the central Mn ion to the base pair is greatly weakened ($J_{23} \approx J_{24} \approx 0$), which corresponds to the limit of two uncoupled dimers.

Importantly, these results together with the results on ammonia binding and the $g4$ /multiline interconversion can all be explained by changes to the bridging ligands between the central and base Mn ions (i.e. J_{23} and J_{24}). Hence, the predicted S -state-dependent conversion of the oxo/hydroxo/aqua ligands at these positions serves to identify these positions as the most likely candidates for the two substrate water sites.

Thus, the funnel model in Fig. 8 meets all of the EPR constraints (1–5). It accounts for the diversity of the S_2 state EPR signals, both their electronic spin multiplicity and their characteristic Mn spin density distributions and the energy gap to the first excited state. The funnel model uses reasonable anti-ferromagnetic J -couplings typical of oxo/hydroxo-bridged Mn ions and does not require physically implausible ferromagnetic couplings between any pairs of Mn ions. The funnel core structure **4** is one of two core types that we put forward as the most likely core type for the Mn_4 cluster of the WOC.

$\text{Mn}_4\text{O}_2(\text{X})_2$ cubane/butterfly cores

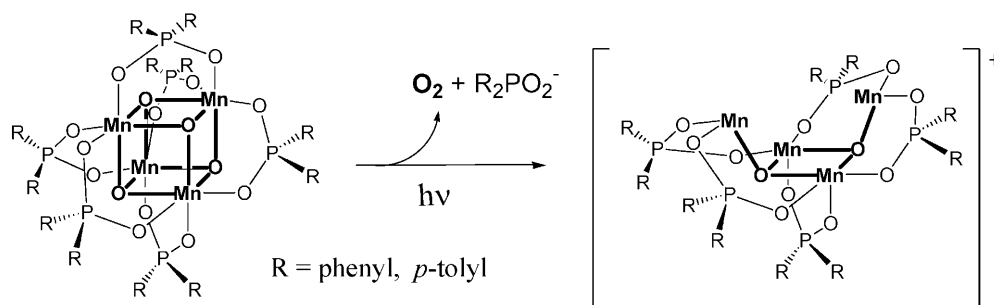
The butterfly/tetrahedron magnetic models presented in Fig. 7, corresponding to the butterfly-cubane structures **11** and **12** (Fig. 5), are also well suited to describing all of the different EPR signals of the S_2 state. The butterfly core **11** has several examples of relevant model complexes for comparison. The complex $\text{Mn}_4\text{O}_2(\text{MeCO}_2)_6(\text{bpy})_2$ has a nearly planar $[\text{Mn}_4\text{O}_2]^{6+}$ core and an intermediate-spin ground state ($S = 2$) resulting from spin frustration between the base Mn(III) and wingtip

Mn(II) ions [65, 123]. For the same reason, complexes containing the nearly planar $[\text{Mn}_4\text{O}_2]^{8+}$ core with all Mn(III) ions also possess an intermediate-spin ground state ($S = 3$) [65]. In both cases, the intermediate-spin ground state arises due to stronger “base” coupling ($J_{34} = -47 \text{ cm}^{-1}$ and $J = -15.6 \text{ cm}^{-1}$) [124] in the nearly planar geometry of these Mn_4O_2 cores (Fig. 7).

The molecule $\text{Mn}_4\text{O}_2(\text{Ph}_2\text{PO}_2)_6$ ($\text{Ph}_2\text{PO}_2^- = \text{diphenylphosphinate}$) is obtained from the cubane $\text{Mn}_4\text{O}_4(\text{Ph}_2\text{PO}_2)_6$ by reductive dehydration of two water molecules from the corners of the cube (see Fig. 10) [125]. NMR and mass spectral data indicate that the $[\text{Mn}_4\text{O}_2]^{6+}$ core appears to have an incomplete cubane structure, equivalent to an acutely bent butterfly core in which the wingtip Mn(II) ions are bridged by one of the six phosphinate chelates in what is called a “pinned butterfly”. EPR data reveal that the two wingtip Mn(II) ions in this complex are electronically isolated Mn(II) ions ($S = 5/2$), with essentially no exchange coupling between them, while the base Mn(III) ions are strongly coupled and essentially diamagnetic ($|J_{34}| \gg |J| \approx |J_{12}| \approx 0$). Cl^- ions readily displace water molecules that bind to the two wingtip Mn(II) ions, presumably at the two open coordination sites at the corners of the cube.

Addition of one or two additional oxo bridges or other inorganic ligands (Cl^- , OH^- , H_2O) between the wingtip Mn ions of the acutely bent butterfly creates the trigonal core $\text{Mn}_4\text{O}_3\text{X}$ and the distorted cuboidal core $\text{Mn}_4\text{O}_2\text{XY}$, illustrated as structures **8** and **12** in Fig. 5, respectively. The case for $\text{X} = \text{Y} = \text{O}$ is realized by the symmetrical cubane complex, $\text{Mn}_4\text{O}_4(\text{Ph}_2\text{PO}_2)_6$, which is diamagnetic with a low-spin ground state ($S = 0$) [69]. The EPR spectrum of the one-electron reduced complex, containing $\text{Mn}_4(3\text{III,IV})$, has a low-spin ground state ($S = 1/2$) with large spin density distributed on all four Mn ions, similar to that observed in the S_2 state $g2$ multiline signal [126]. The distorted cubane core type **12** is particularly well suited as an S_2 state model because it possesses the correct exchange symmetry to produce all four of the observed spin states and their associated Mn hyperfine spin densities, as described in Fig. 7. Moreover, it does this without assuming physically unrealistic ferromagnetic couplings between any of the Mn ions. Conversion of cubane **12** to the acutely bent butterfly core **11** by removal of two X bridges (or replacement by water) is predicted to occur upon two-electron reduction

Fig. 10 O_2 production by photo-rearrangement of $\text{L}_6\text{Mn}_4\text{O}_4$. The $[\text{Mn}_4\text{O}_4]^{6+}$ “cubane” core rearranges to the $[\text{Mn}_4\text{O}_2]^{6+}$ “butterfly” core [148]



to the S_0 level, $Mn_4(II,3III)$. This geometry should preserve a low-spin ground state ($S=1/2$) and thus also be compatible with the electronic spin state for the S_0 state (Table 1). This conversion is analogous to the conversion of the cubane $L_6Mn_4O_4$ to the pinned butterfly $L_6Mn_4O_2$ described above.

The cubane core **12** is also suitable to describe the characteristic dimer-like $Mn_2(II,III)$ EPR signal formed upon reduction of S_1 by excess NO gas [122]. In Fig. 7 (upper right corner), the cubane core with Mn(II) at position 4 and with couplings ($J_{12}=-0.8$, $J_{13}=J_{23}=-0.4$, $J_{14}=J_{24}=-0.2$, $J_{34}=-0.2$) produces a ground $S=1/2$ state with spin density (0.0, 0.0, -1.33, 2.33) that resides exclusively on two Mn ions comprising a $Mn_2(II,III)$ pair, while the other two Mn ions form a diamagnetic $Mn_2(III,III)$ pair ($S_{12}=0$) that carries no spin density. Mirror symmetry in the cubane core (i.e. $J_{13}=J_{23}$ and $J_{14}=J_{24}$) is essential to produce this spin density distribution, except when these couplings become much smaller than the intra-dimer couplings (J_{12} , $J_{34} \gg J_{ij}$). However, each J_{ik} coupling can be varied significantly (by 25–50%) and still result in the same ground state and zero spin density on two of the Mn ions. This model is obtained from the butterfly by introducing a strong coupling between the “wingtip” Mn ions (J_{12}). Thus, the butterfly-cubane magnetic model is one of two models that accounts for the full range of EPR signals observed in PSII.

Structural models of the Mn_4Ca core

The previously described EPR and XAS data, together with the photoactivation kinetics during Mn_4 core assembly [5], indicate a close association between Ca and Mn in the WOC. Sr EXAFS provides the most direct evidence locating the Sr^{2+} (Ca^{2+}) at a distance of 3.3–3.6 Å to Mn. In Fig. 9 we illustrate four candidates for the location of Ca^{2+} relative to the Mn_4 core, using the two most favored Mn_4 core geometries. They may be described as two isomers of a calcium-capped Mn_4O_6 -funnel core and two isomers of a calcium-capped $Mn_4O_2Y_2$ -cuboidal core. These structures locate Ca^{2+} at a peripheral site that bridges between two Mn atoms and preserve C_2 or C_s symmetry of the electron spin density. The identity of the bridging ligands (X) between Ca and Mn is not known with certainty. Candidates include chloride and oxygen-based ligands based on preferences seen in small-molecule complexes. Boldface symbols in Fig. 9 identify bridging ligand sites that are responsible for changes in the inter-Mn spin coupling and ground spin state. These also identify possible substrate water sites.

S_0 state EPR

The S_0 state multiline EPR signal has much weaker intensity and $\geq 15\%$ broader spectral breadth (more than

2200 G) compared to the S_2 state signal (Table 1) [127, 128, 129]. It is centered at $g \approx 2$ and has at least 20 resolved lines (observed only in the presence of methanol) from ^{55}Mn hyperfine structure with an average splitting of 82 G; more lines should be resolved in the wings as sensitivity improvements are discovered for this new signal. The signal was determined to originate from an electronic ground $S=1/2$ state [130, 131]. The predicted oxidation ground state for S_0 should be $Mn_4(II,3III)$ if the favored assignment of S_2 as $Mn_4(3III,IV)$ proves to be correct. Both theoretical and experimental evidence from model complexes shows that this oxidation state produces a larger hyperfine interaction and thus larger spectral breadth by about 20–25% compared to the S_2 multiline spectrum [99, 132, 133]. No additional information on Mn coordination number or cluster symmetry has been suggested yet for the S_0 WOC, since accurate EPR spectral simulations are not yet possible owing to limited sensitivity and poor resolution. However, since Mn EXAFS has indicated a structural similarity between S_0 and S_2 [28, 57], the funnel, butterfly, or tetrahedral magnetic models, illustrated by cores **2**, **4**, **7–9**, and **11–13** (Fig. 5), should still be favored for the S_0 state Mn_4 core topology.

S_1 state EPR

The S_1 state is detectable by EPR only using parallel-mode microwave excitation. A broad signal with unresolved hyperfine structure at $g=4.8$ [134, 135] and, more recently, a “multiline” signal centered at $g=12$ with 19–21 resolved lines due to ^{55}Mn hyperfine structure have been reported [136, 137]. The ^{55}Mn hyperfine splitting is highly regular with all splittings essentially identical (32 G). The peaks exhibit an ascending pattern of intensities, indicating a high spectral density of degenerate nuclear states, indicative of a tetramanganese cluster. The $g4.8$ signal has been observed in spinach PSII membranes, whereas the $g12$ “multiline” signal has been detected in spinach core complexes only after removal of the 23 kDa and 17 kDa extrinsic proteins of the WOC. By contrast, only the $g12$ multiline form is detected in cyanobacteria, which lacks these two proteins in the genome. Despite the two different S_1 signals, the conventional (perpendicular-mode) multiline S_2 signal was produced upon illumination of both these preparations, demonstrating S-state transition and an intact geometry of the Mn_4 cluster. Therefore, the two S_1 signals should be considered as two “native” forms of the S_1 state.

Both the $g4.8$ and the $g12$ multiline signals of S_1 were interpreted as due to an integer spin cluster, with $S \geq 1$. A low-lying $S=1$ excited state was suggested for the $g4.8$ signal (above a diamagnetic ground state $S=0$), while a ground (or low-lying excited) state with spin $S=1$ or 2 was suggested for the $g12$ signal. It is important to recognize that none of the integer spin assignments for any of the S_1 signals have been corroborated by EPR at two

or more frequencies nor by spin nutation studies. Hence, the proposed values of these integer spin states are arbitrary and should be viewed as suggestive only. In either case, a lower spin assignment of the ground state is suggested ($S=0-2$), and thus the Mn_4 cluster has an anti-ferromagnetic core in the S_1 state. Possible Mn oxidation states for S_1 that can be considered are $Mn_4(4III)$ and $Mn_4(2III,2IV)$. The latter oxidation state could have either delocalized or trapped valences, provided the inter-manganese exchange couplings preserve equal spin projections for the four Mn ions.

The “multiline” structure observed on the g_{12} signal has been argued to require that all four (or at least three) Mn ions are exchange-coupled in the WOC [137]. The EPR spectrum has been simulated assuming equivalent hyperfine couplings on all four Mn ions [71]. This imposes specific requirements on the geometry of the cluster in order to preserve a high symmetry for the spin exchange interactions. The possible core models are the funnel, butterfly, or tetrahedron magnetic models (Fig. 5, cores **2**, **4**, **7-9**, **11-13**) [104, 138]. These give rise to the essential spin frustration needed for creation of a low-to-intermediate-spin ground (or low-lying excited) state having $S=1$ or 2 and equal spin density on each of the Mn ions.

There appears to be no definitive way of eliminating either of the two possible oxidation state assignments, $Mn_4(4III)$ or $Mn_4(2III,2IV)$, based on the presently available data. However, the simplest interpretation having the fewest ad hoc assumptions favors the former choice of $Mn_4(4III)$.

S_3 state EPR

For the native S_3 state, low-field EPR peaks at $g=6.7$ (perpendicular mode) and $g=8-12$ (parallel mode) have been detected [139, 140]. The signals show no ^{55}Mn hyperfine structure and were fitted to a model assuming a low-lying excited state ($S=1$) with moderate zero-field splitting interaction, although other integer spin values were not excluded. Matsukawa et al. [139] favored that the Mn_4 cluster is oxidized either to $Mn_4(2III,2IV)$ or $Mn_4(4IV)$ to explain these signals. However, oxidation of a nearby amino acid residue that is coupled anti-ferromagnetically to an odd spin of the S_2 state would also fit the structureless EPR signal. On near-IR illumination at 50 K, the S_3 signals are transformed in part to a split signal centered at $g=2$ and detected with conventional perpendicular-mode EPR [140]. The latter signal closely resembles the “split-radical” signals detected in modified PSII centers after acetate-treatment, Ca^{2+} removal, or replacement of Cl^- by F^- [36, 141, 142]. These samples are blocked at the S_3 level against further turnover. The “split” S_3 signal has been convincingly simulated by a model in which the Mn_4 cluster in its g_2 multiline S_2 state is coupled to a protein-derived radical [143, 144, 145]. There is agreement that the radical is tyrosine Y_z in the majority of sample

preparations [143, 146]. This inhibited state is designated as $S_2Y_z^\bullet$ (Table 1).

The lack of resolved hyperfine structure on the S_3 signal limits structural conclusions about the Mn_4 core. The suggested description of a diamagnetic ground state ($S=0$) and triplet first-excited state ($S=1$) separated by a small energy gap (2.4 cm^{-1}) [139] is plausible, but not unique, and requires confirmation by multi-frequency experiments. If correct, this assignment indicates an anti-ferromagnetic spin-frustrated Mn_4 core. The funnel, acutely bent butterfly, or tetrahedron magnetic models for the Mn_4 cluster are consistent with this assignment.

Proposed Mn_4 core types for O_2 evolution based on functional model systems

In this final section we highlight two core types, **4** and **12**, among the eight core types allowed by the XAS/EPR constraints. These are particularly promising candidates for catalysis of O_2 production in the WOC based on demonstrated O_2 evolution chemistry in related model systems.

Mn_4O_4 -cubane-to- Mn_4O_2 -butterfly

A cubane/butterfly core rearrangement, represented by cores **11** and **12**, was proposed in an early hypothesis for the photosynthetic O_2 evolution step [147]. The feasibility of this rearrangement was recently demonstrated in a model cluster, as summarized in Fig. 10 [148]. The molecule $Mn_4O_4(Ph_2PO_2)_6$ contains a symmetrical $[Mn_4O_4]^{6+}$ core. UV light absorption efficiently releases an O_2 molecule in the gas phase and one of the phosphinate chelates, leaving the cationic species $[Mn_4O_2(Ph_2PO_2)_5]^+$ (presumed Mn_4O_2 butterfly core). This reaction proceeds with high quantum efficiency ($> 50\%$), is the only observable reaction channel (other than decay to the ground state), and is selective to the cubane core type (i.e. not observed for Mn_2O_2 , Mn_2O , or Mn_3O_4 cores) [149].

Photo-production of O_2 from permanganate

Another Mn-oxo complex that has been proven to undergo O_2 evolution is permanganate, MnO_4^- (reviewed in [18]). A study conducted by Lee et al. [150] found that the photo-reaction proceeds in solution by direct formation of MnO_2^- and O_2 as the initial products and was interpreted by the mechanism shown in Fig. 11.

A tetrahedral MnO_4 core is found at the center of the “funnel” core type **4** in Fig. 5. We speculate that this core type represents a potential catalytic geometry suited for intramolecular O-O bond formation and O_2 evolution in the S_4 state via thermally activated electron transfer to the peripheral Mn ions. Direct experimental evidence for such a ground state pathway is lacking,

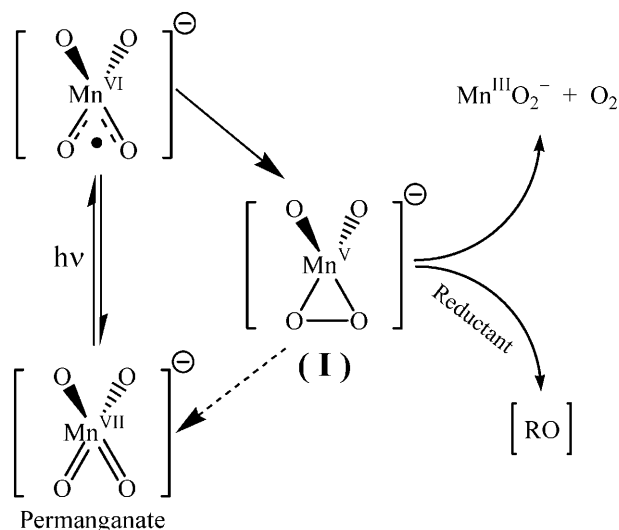


Fig. 11 Charge transfer photo-excitation of permanganate leads to intramolecular O_2 production via a peroxo intermediate “I” [150]

perhaps because no model complexes having this core type have been synthesized to test the concept.

The reactions in Figs. 10 and 11 suggest two interesting possibilities to consider for the photosynthetic O_2 evolution step. In the future, when an atomic resolution structure of the WOC becomes available, it will be helpful to consider these functional models in formulating mechanistic hypotheses.

Acknowledgements We thank Drs. A. Boussac, C. Berthoumieu, R.D. Britt, and W. Hillier for helpful comments and unpublished data, and A. Kawamori and V. Petrouleas for preprints of their work. Unpublished XANES data were kindly provided by Dr. V. Yachandra. This work was supported by the National Institutes of Health (grant GM-39932).

References

- Joliet P (1993) *Photosynth Res* 38:214–223
- Dismukes GC, Siderer Y (1981) *Proc Natl Acad Sci USA* 78:274–278
- Dismukes GC, Ferris K, Watnick P (1982) *Photobiochem Photobiophys* 3:243–256
- Debus RJ (1992) *Biochim Biophys Acta* 1102:269–352
- Ananyev GM, Zaltsman L, Vasko C, Dismukes GC (2001) *BBA Bioenergetics* 1503:52–68
- Barry B, Babcock GT (1987) *Proc Natl Acad Sci USA* 84:7099–7103
- Rappaport F, Lavergne J (2001) *BBA Bioenergetics* 1503:246–259
- Tommos C, Babcock GT (1998) *Acc Chem Res* 31:18–25
- Haumann M, Junge W (1999) *BBA Bioenergetics* 1411:86–91
- Debus R (2001) *BBA Bioenergetics* 1503:164–186
- Renger G, Christen G, Karge M, Eckert H-J, Irrgang K-D (1998) *JBIC* 3:360–366
- Zouni A, Witt H-T, Kern J, Fromme P, Krauss N, Sanger W, Orth P (2001) *Nature* 409:739–743
- Barber J, Nield J, Morris EP, Hankamer B (1999) *Trends Biochem Sci* 24:42–45
- Dismukes GC (2001) *Science* 292:447
- Rutherford AW, Faller P (2001) *Trends Biochem Sci* 26:341–344
- Hoganson CW, Babcock GT (1997) *Science* 277:1953–1955
- Diner BA, Force DA, Randall DW, Britt RD (1998) *Biochemistry* 37:17931–17943
- Ruettinger W, Dismukes GC (1997) *Chem Rev* 97:1–24
- Koningsberger DC, Prins R (1988) *X-ray absorption: principles, applications, and techniques of EXAFS, SEXAFS, and XANES*, Wiley-Interscience, New York
- Yachandra VK (1995) *Methods Enzymol* 246:638–675
- Scott RA (2000) In: Que L Jr (ed) *Physical methods in bioinorganic chemistry*. University Science Press, Menlo Park, pp 465–503
- Sauer K, Yachandra VK, Britt RD, Klein MP (1992) In: Pecoraro VL (ed) *Manganese redox enzymes*. VCH, New York, pp 141–175
- Roelofs TA, Liang W, Latimer MJ, Cinco RM, Rompel A, Andrews JC, Sauer K, Yachandra VK, Klein MP (1996) *Proc Natl Acad Sci USA* 93:3335–3340
- Ono T, Noguchi T, Inoue Y, Kusunoki M, Matsushita T, Oyanagi H (1992) *Science* 258:1335–1337
- Iuzzolino L, Dittmer J, Dorner W, Meyer-Klaucke W, Dau H (1998) *Biochemistry* 37:17112–17119
- Liang W, Roelofs TA, Cinco RM, Rompel A, Latimer MJ, Yu WO, Sauer K, Klein MP, Yachandra YK (2000) *J Am Chem Soc* 122:3399–3412
- Yachandra VK, DeRose VJ, Latimer MJ, Mukerji I, Sauer K, Klein MP (1993) *Science* 260:675–679
- Yachandra VK, Sauer K, Klein MP (1996) *Chem Rev* 96:2927–2950
- Riggs PJ, Mei R, Yocum CF, Penner-Hahn JE (1992) *J Am Chem Soc* 114:10650–10651
- Kusunoki M, Ono T, Noguchi T, Inoue Y, Oyanagi H (1993) *Photosynth Res* 38:331–339
- Cinco RM, Rompel A, Visser H, Aromi G, Christou G, Sauer K, Klein MP, Yachandra VK (1999) *Inorg Chem* 38:5988–5998
- Yocum CF (1991) *Biochim Biophys Acta* 1059:1–15
- Ghanotakis DF, Babcock GT, Yocum CF (1984) *Biochim Biophys Acta* 765:388–398
- Boussac A, Rutherford AW (1988) *Biochemistry* 27:3476–3483
- Ghanotakis D, Babcock GT, Yocum CF (1985) *Biochim Biophys Acta* 809:173–180
- Boussac A, Zimmerman J-L, Rutherford AW (1989) *Biochemistry* 28:8984–8989
- Sivaraja M, Tso J, Dismukes GC (1989) *Biochemistry* 28:9459–9464
- Tso J, Sivaraja M, Dismukes CD (1991) *Biochemistry* 30:4734–4739
- Latimer MJ, DeRose VJ, Yachandra VK, Sauer K, Klein MP (1998) *J Phys Chem B* 102:8257–8265
- Ono T, Kusunoki M, Matsushita T, Oyanagi H, Inoue Y (1991) *Biochemistry* 30:6836–6841
- Ono T, Noguchi T, Inoue Y, Kusunoki M, Yamaguchi H, Oyanagi H (1993) *FEBS Lett* 330:28–30
- Latimer MJ, DeRose VJ, Mukerji I, Yachandra VK, Sauer K, Klein MP (1995) *Biochemistry* 34:10898–10909
- Riggs-Gelasco PJ, Mei R, Ghanotakis DF, Yocum CF, Penner-Hahn JE (1996) *J Am Chem Soc* 118:2400–2410
- Glaser T, Hedman B, Hodgson KO, Solomon EI (2000) *Acc Chem Res* 33:859–868
- NIST (2001) *NIST chemistry webbook*. (Standard reference database 69) US Secretary of Commerce, Washington, <http://webbook.nist.gov/chemistry>
- Bergmann U, Grush MM, Horne CR, DeMarois P, Penner-Hahn JE, Yocum CF, Wright DW, Dube CE, Armstrong WH, Christou G, Eppley HJ, Cramer SP (1998) *J Phys Chem B* 102:8350–8352
- Robblee JH, Cinco RM, Yachandra VK (2001) *BBA Bioenergetics* 1503:7–23
- DeRose VJ, Mukerji I, Latimer MJ, Yachandra VK, Sauer K, Klein MP (1994) *J Am Chem Soc* 116:5239–5249
- DeRose VJ, Yachandra VK, McDermott AE, Britt RD, Sauer K, Klein MP (1991) *Biochemistry* 30:1335–1341

50. Penner-Hahn JE, Fronko RH, Pecoraro VL, Yocum CF, Betts SD, Bowlby NR (1990) *J Am Chem Soc* 112:2549–2557
51. Sheats JE, Czernuziewicz R, Dismukes GC, Rheingold A, Petrouleas V, Stubbe J, Armstrong WH, Beer R, Lippard SJ (1987) *J Am Chem Soc* 109:1435–1444
52. Mandal SK, Armstrong WH (1995) *Inorg Chim Acta* 229:261–270
53. Dave BC, Czernuszewicz RS (1998) *Inorg Chim Acta* 281:25–35
54. Wieghardt K, Bossek U, Bonvoisin J, Beauvillain P, Girerd JJ, Nuber B, Weiss J, Heinze J (1986) *Angew Chem Int Ed Engl* 25:1030–1031
55. Dave BC, Czernuszewicz RS, Bond MR, Carrano CJ (1993) *Inorg Chem* 32:3593–3594
56. Mukerji I, Andrews JC, DeRose VJ, Latimer MJ, Yachandra VK, Sauer K, Klein MP (1994) *Biochemistry* 33:9712–9721
57. Riggs-Gelasco PJ, Mei R, Yocum CF, Penner-Hahn JE (1996) *J Am Chem Soc* 118:2387–2399
58. Guiles RD, Yachandra VK, McDermott AE, Cole JL, Dexheimer SL, Britt RD, Sauer K, Klein MP (1990) *Biochemistry* 29:486–496
59. Bashkin JS, Chang H-R, Streib WE, Huffman JC, Hendrickson DN, Christou G (1987) *J Am Chem Soc* 109:6502–6504
60. Wang S, Folting K, Streib WE, Schmitt EA, McCusker JK, Hendrickson DN, Christou G (1991) *Angew Chem Int Ed Engl* 30:305–306
61. Wemple MW, Adams DM, Folting K, Hendrickson DN, Christou G (1995) *J Am Chem Soc* 117:7275–7276
62. Aromi G, Aubin MJ, Bocar MA, Christou G, Eppley HJ, Folting K, Hendrickson DN, Huffman JC, Squire RC, Tsai H-L, Wang S, Wemple MW (1998) *Polyhedron* 17:3005–3020
63. Hendrickson DN, Christou G, Schmitt EA, Libby E, Bashkin JS, Wang S, Tsai H-L, Vincent JB, Boyd PDW, Huffman JC, Folting K, Li W, Streib WE (1992) *J Am Chem Soc* 114:2455–2471
64. Wang SY, Tsai HL, Libby E, Folting K, Streib WE, Hendrickson DN, Christou G (1996) *Inorg Chem* 35:7578–7589
65. Vincent JB, Christmas C, Chang H-R, Li Q, Boyd PDW, Huffman JC, Hendrickson DN, Christou G (1989) *J Am Chem Soc* 111:2086–2097
66. Libby E, McCusker JK, Schmitt EA, Folting K, Hendrickson DN, Christou G (1991) *Inorg Chem* 30:3486–3495
67. Libby E, Folting K, Huffman CJ, Huffman JC, Christou G (1993) *Inorg Chem* 32:2549–2556
68. Kulawiec RJ, Crabtree RH, Brudvig GW, Schulte GK (1988) *Inorg Chem* 27:1309–1311
69. Ruettinger W, Campana C, Dismukes GC (1997) *J Am Chem Soc* 119:6670–6671
70. Ruettinger WF, Ho DM, Dismukes GC (1999) *Inorg Chem* 38:1036–1037
71. Britt RD, Peloquin JM, Campbell KA (2000) *Annu Rev Biophys Biomol Struct* 29:463–495
72. Hansson O, Andreasson L-E (1982) *Biochim Biophys Acta* 679:261–268
73. Casey JL, Sauer K (1984) *Biochim Biophys Acta* 767:21–28
74. Zimmermann J-L, Rutherford AW (1984) *Biochim Biophys Acta* 767:7507–7511
75. Kim DH, Britt RD, Klein MP, Sauer K (1992) *Biochemistry* 31:541–547
76. Boussac A, Rutherford AW (2000) *BBA Bioenergetics* 1457:145–156
77. Boussac A, Un S, Horner O, Rutherford AW (1998) *Biochemistry* 37:4001–4007
78. Aasa R, Hansson O, Vanngard T (1987) In: Biggins J (ed) *Progress in photosynthesis research*. Nijhoff, Dordrecht, pp 577–581
79. Pace RJ, Smith P, Bramley R, Stehlik D (1991) *Biochim Biophys Acta* 1058:161–170
80. Britt RD, Lorigan GA, Sauer K, Klein MP, Zimmermann JL (1992) *Biochim Biophys Acta* 1140:95–101
81. Haddy A, Dunham WR, Sands RH, Aasa R (1991) *Biochim Biophys Acta* 1099:25–34
82. Astashkin AV, Kodera Y, Kawamori A (1994) *J Magn Reson B* 105:113–119
83. Horner O, Riviere E, Blondin G, Un S, Rutherford AW, Girerd JJ, Boussac A (1998) *J Am Chem Soc* 120:7924–7928
84. Hanson GR, Wilson GL, Bailey TD, Pilbrow JR, Wedd AG (1987) *J Am Chem Soc* 109:2609–2616
85. Ahrling KA, Smith PJ, Pace RJ (1998) *J Am Chem Soc* 120:13202–13214
86. Dismukes G, Mathis P (1984) *FEBS Lett* 178:51–54
87. Baxter R, Krausz E, Wydrzynski T, Pace R (1999) *J Am Chem Soc* 121:9451–9452
88. Renger G (2001) *BBA Bioenergetics* 1503:210–228
89. Liang W, Latimer MJ, Dau H, Roelofs TA, Yachandra VK, Sauer K, Klein MP (1994) *Biochemistry* 33:4923–4932
90. Onoda K, Mino H, Inoue Y, Noguchi T (2000) *Photosynth Res* 63:47–57
91. Dismukes GC (1988) *Chem Scr* 28a:99–104
92. Dismukes GC (1991) In: Prassides K (ed) *Mixed valency systems: applications in chemistry, physics and biology*. Kluwer, Dordrecht, pp 137–154
93. Bonvoisin J, Blondin G, Girerd JJ, Zimmermann JL (1992) *Biophys J* 61:1076–1086
94. Ahrling KA, Pace RJ (1995) *Biophys J* 68:2081–2090
95. Zheng M, Dismukes GC (1996) *Inorg Chem* 35:3307–3319
96. Peloquin JM, Campbell KA, Randall DW, Evanchik MA, Pecoraro VL, Armstrong WH, Britt RD (2000) *J Am Chem Soc* 122:10926–10942
97. Hasegawa K, Kusunoki M, Inoue Y, Ono TA (1998) *Biochemistry* 37:9457–9465
98. Lakshmi KV, Eaton SS, Eaton GR, Brudvig GW (1999) *Biochemistry* 38:12758–12767
99. Zheng M, Khangulov SV, Dismukes GC, Barynin VV (1994) *Inorg Chem* 33:382–387
100. Ono T-A, Inoue Y (1990) In: Baltischeffsky M (ed) *Current research in photosynthesis*. Kluwer, Dordrecht, pp 701–708
101. Zaltsman L, Ananyev G, Bruntrager E, Dismukes GC (1997) *Biochemistry* 36:8914–8922
102. Ananyev GM, Dismukes GC (1996) *Biochemistry* 35:4102–4109
103. Ananyev GM, Dismukes GC (1997) *Biochemistry* 36:11342–11350
104. Bencini C, Gatteschi D (1990) *EPR of exchange coupled systems*. Springer, Berlin Heidelberg New York
105. Belinskii MI (1994) *Chem Phys* 179:1–22
106. Blondin G, Davydov R, Philouze C, Charlot M-F, Styring S, Åkermark B, Girerd J-J, Boussac A (1997) *J Chem Soc Dalton Trans* 4069–4074
107. Kessissoglou DP (1999) *Coord Chem Rev* 186:837–858
108. Law NA, Kampf JW, Pecoraro VL (2000) *Inorg Chim Acta* 297:252–264
109. Manchandra R, Brudvig GW, Crabtree RH (1995) *Coord Chem Rev* 144:1–38
110. Gultneh Y, Ahvazi B, Khan AR, Butcher RJ, Tuchagues JP (1995) *Inorg Chem* 34:3633–3645
111. Caneschi A, Gatteschi D, Sessoli R (1997) *J Chem Soc Dalton Trans* 3963–3970
112. Duboc-Toia C, Hummel H, Bill E, Barra A-L, Chouteau G, Wieghardt K (2000) *Angew Chem Int Ed* 39:2888–2890
113. Wang SY, Wemple MS, Yoo J, Folting K, Huffman JC, Hagen KS, Hendrickson DN, Christou G (2000) *Inorg Chem* 39:1501–1513
114. Hotselmann R, Wieghardt R (1993) *Inorg Chem* 32:114–116
115. Hasegawa K, Ono TA, Inoue Y, Kusunoki M (1999) *Chem Phys Lett* 300:9–19
116. Belinskii MI (1994) *Chem Phys* 189:451–465
117. Hasegawa K, Ono T, Inoue Y, Kusunoki M (1999) *Bull Chem Soc Jpn* 72:1013–1023
118. Britt RD, Zimmermann JL, Sauer K, Klein MP (1989) *J Am Chem Soc* 111:3522–3532
119. Sarneski JE, Thorp HH, Brudvig GW, Crabtree RH, Schulte GK (1990) *J Am Chem Soc* 112:7255–7260

120. Auger N, Girerd JJ, Corbella M, Gleizes A, Zimmermann JL (1990) *J Am Chem Soc* 112:448–450
121. Pal S, Chan MK, Armstrong WH (1992) *J Am Chem Soc* 114:6398–6406
122. Sarrou J, Ionnidis N, Deligiannakis Y, Petrouleas V (1998) *Biochemistry* 37:3581–3587
123. Thorp H, Brudvig GW (1991) *New J Chem* 15:479–490
124. Vincent JB, Chang HR, Folting K, Huffman JC, Christou G, Hendrickson DN (1987) *J Am Chem Soc* 109:5703
125. Ruettinger WF, Dismukes GC (2000) *Inorg Chem* 39:1021–1027; correction: 39:4186
126. Dismukes GC, Ruettinger W, Boelrijk AEM, Ho D (1998) In: Garob G (ed) *Proceedings of the XIth international photosynthesis congress*. Kluwer, Dordrecht, pp 1259–1264
127. Messinger J, Nugent-JHA, Evans-MCW (1997) *Biochemistry* 37:11055–11060
128. Ahrling KA, Peterson S, Styring S (1997) *Biochemistry* 36:13148–13152
129. Boussac A, Kuhl H, Ghibaudi E, Rogner M, Rutherford AW (1999) *Biochemistry* 38:11942–11948
130. Ahrling KA, Peterson S, Styring S (1998) *Biochemistry* 37:8115–8120
131. Peterson S, Ahrling KA, Styring S (1999) *Biochemistry* 38:15223–15230
132. Dismukes GC, Sheats JE, Smegal JA (1987) *J Am Chem Soc* 109:7202–7203
133. Geijer P, Peterson S, Ahrling KA, Deak Z, Styring S (2001) *BBA Bioenergetics* 1503:83–95
134. Dexheimer SL, Klein MP (1992) *J Am Chem Soc* 114:2821–2826
135. Yamauchi T, Mino H, Matsukawa T, Kawamori A, Ono T (1997) *Biochemistry* 36:7520–7526
136. Campbell KA, Gregor W, Pham DP, Peloquin JM, Debus RJ, Britt RD (1998) *Biochemistry* 37:5039–5045
137. Campbell KA, Peloquin JM, Pham DP, Debus RJ, Britt RD (1998) *J Am Chem Soc* 120:447–448
138. Belinskii MI (1994) *Chem Phys* 179:1–22
139. Matsukawa T, Mino H, Yoneda D, Kawamori A (1999) *Biochemistry* 38:4072–4077
140. Ioannidis N, Petrouleas V (2000) *Biochemistry* 39:5246–5254
141. Maclachlan DJ, Nugent JHA (1993) *Biochemistry* 32:9772–9780
142. Baumgarten M, Philo JS, Dismukes GC (1990) *Biochemistry* 29:10814–10822
143. Peloquin JM, Campbell KA, Britt RD (1998) *J Am Chem Soc* 120:6840–6841
144. Lakshmi KV, Eaton SS, Eaton GR, Frank HA, Brudvig GW (1998) *J Phys Chem B* 102:8327–8335
145. Dorlet P, Boussac A, Rutherford AW, Un S (1999) *J Phys Chem B* 103:10945–10954
146. Astashkin AV, Mino H, Kawamori A, Ono TA (1997) *Chem Phys Lett* 272:506–516
147. Vincent JB, Christou G (1987) *Inorg Chim Acta* 136:L41–L43
148. Ruettinger W, Yagi M, Wolf K, Bernasek S, Dismukes GC (2000) *J Am Chem Soc* 122:10353–10357
149. Yagi M, Wolf KV, Baesjou PJ, Bernasek SL, Dismukes GC (2001) *Angew Chem Int Ed* 40:2925–2928
150. Lee DG, Moylan CR, Hayashi T, Brauman JI (1987) *J Am Chem Soc* 109:3003–3010
151. Boussac A, Girerd J-J, Rutherford AW (1996) *Biochemistry* 35:6984–6989
152. Beck WF, de Paula JC, Brudvig GW (1986) *J Am Chem Soc* 108:4018–4022
153. Lorigan GA, Britt RD (1994) *Biochemistry* 33:12072–12076
154. Koulouglotis D, Schweitzer RH, Brudvig GW (1997) *Biochemistry* 36:9735–9746